Article

Shedding Light on the Inhibitory Mechanisms of SARS-CoV-1/CoV-2 Spike Proteins by ACE2-Designed Peptides

Frederico Campos Freitas,[§] Paulo Henrique Borges Ferreira,[§] Denize Cristina Favaro, and Ronaldo Junio de Oliveira*

Cite This: https://dx.doi.org/10.1021/acs.jcim.0c01320

Read Online

ACCESS | 📊 Metrics & More | 📰 Article Recommendations | 🆂🅸 Supporting Information

ABSTRACT: Angiotensin-converting enzyme 2 (ACE2) is the host cellular receptor that locks onto the surface spike protein of the 2002 SARS coronavirus (SARS-CoV-1) and of the novel, highly transmissible and deadly 2019 SARS-CoV-2, responsible for the COVID-19 pandemic. One strategy to avoid the virus infection is to design peptides by extracting the human ACE2 peptidase domain α_1-helix, which would bind to the coronavirus surface protein, preventing the virus entry into the host cells. The natural α_1-helix peptide has a stronger affinity to SARS-CoV-2 than to SARS-CoV-1. Another peptide was designed by joining α_1 with the second portion of ACE2 that is far in the peptidase sequence yet grafted in the spike protein interface with ACE2. Previous studies have shown that, among several α_1-based peptides, the hybrid peptidic scaffold is the one with the highest/strongest affinity for SARS-CoV-1, which is comparable to the full-length ACE2 affinity. In this work, binding and folding dynamics of the natural and designed ACE2-based peptides were simulated by the well-known coarse-grained structure-based model, with the computed thermodynamic quantities correlating with the experimental binding affinity data. Furthermore, theoretical kinetic analysis of native contact formation revealed the distinction between these processes in the presence of the different binding partners SARS-CoV-1 and SARS-CoV-2 spike domains. Additionally, our results indicate the existence of a two-state folding mechanism for the designed peptide en route to bind to the spike proteins, in contrast to a downhill mechanism for the natural α_1-helix peptides. The presented low-cost simulation protocol demonstrated its efficiency in evaluating binding affinities and identifying the mechanisms involved in the neutralization of spike-ACE2 interaction by designed peptides. Finally, the protocol can be used as a computer-based screening of more potent designed peptides by experimentalists searching for new therapeutics against COVID-19.
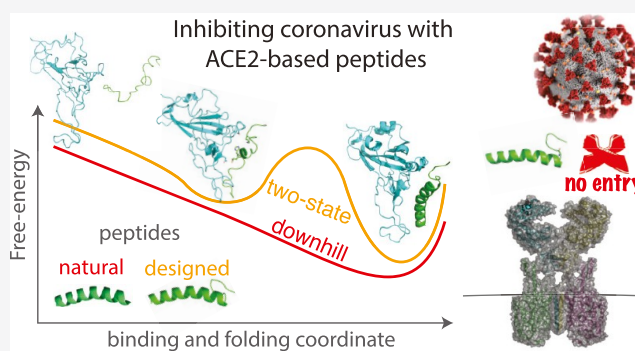
INTRODUCTION

Coronaviruses (CoV) represent a diverse family of single-stranded, positive-sense RNA viruses capable of infecting humans and animals.[1] Historically, coronaviruses have infected humans causing mild cold; however, highly pathogenic strains have emerged over the past two decades.[2−5] In 2002−2003, severe acute respiratory syndrome coronavirus (SARS-CoV-1) infected over 8000 people worldwide, with approximately 800 deaths. In 2012, Middle East respiratory syndrome coronavirus (MERS-CoV), first identified in Saudi Arabia, caused 2500 confirmed cases and a death rate of 36%.[5] Even though a new outbreak of SARS-CoV-1 was expected by 2004, SARS-CoV-1 remained absent from human circulation until December 2019. Compared to SARS-CoV-1 and MERS-CoV, the new strain of coronaviruses (SARS-CoV-2, previously known as 2019-nCoV) spreads more efficiently. According to the World Health Organization (WHO) report, by January 24th of 2021, more than 97.4 million people have been infected worldwide, including more than 2.1 million deaths. Sequencing of the SARS-CoV-2 genome indicates that the 30 kb RNA encodes four structural proteins: spike (S), envelope (E), membrane (M), and nucleocapsid (N); 16 nonstructural proteins (Nsp1-16); and 9 putative accessory factors.[6,7] The trimeric glycosylated spike protein is the key used by both SARS-CoV-1 and SARS-CoV-2 viruses to enter host cells. During viral infection, the trimeric protein is cleaved into S1 and S2 subunits. S1 contains the receptor-binding domain (RBD), which recognizes the peptidase domain (PD) of angiotensin-converting enzyme 2 (ACE2), and S2 is responsible for membrane fusion[3,8,9] (Figures 1A,B, and S1).
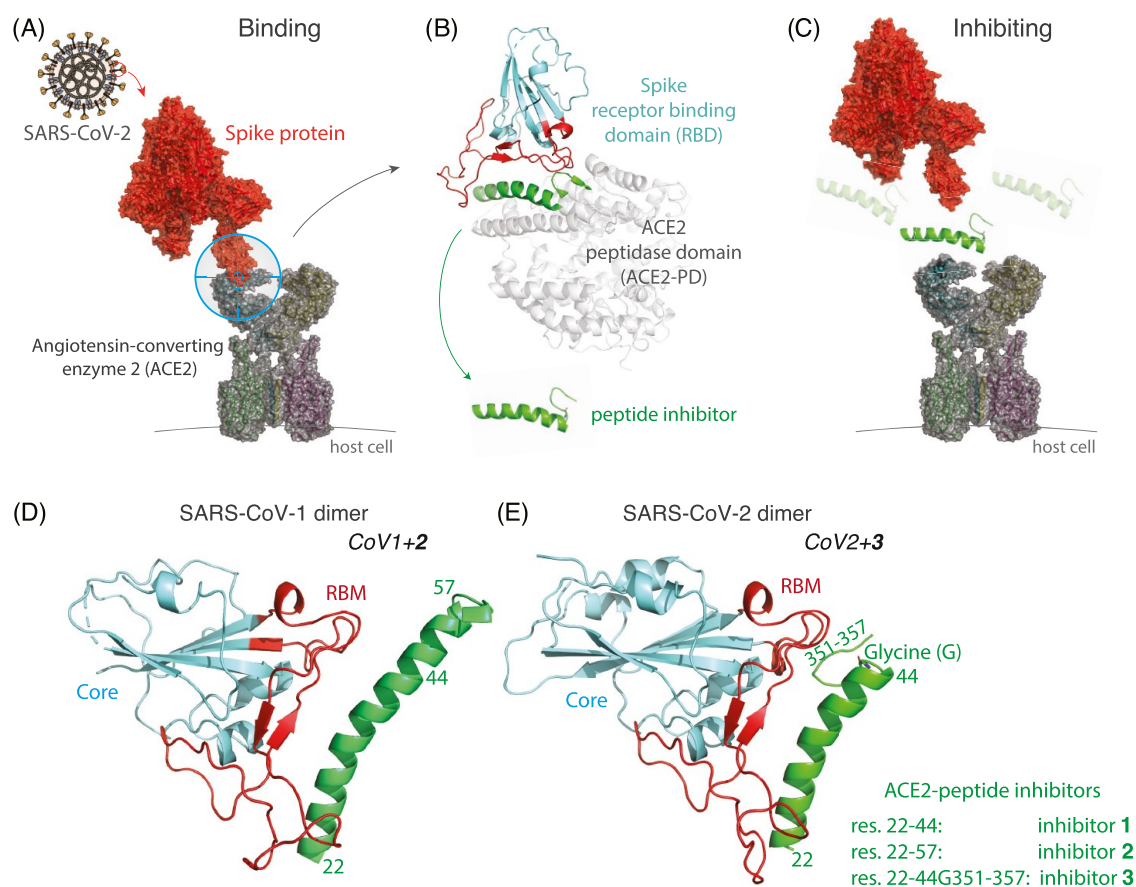
Figure 1. SARS-CoV-1 and SARS-CoV-2 spike proteins inhibited by ACE2-based peptides. (A) Coronavirus uses the surface spike protein (in red) to lock onto human ACE2 receptors (in gray) located on the surface of host cells to deliver its RNA to produce more viruses. (B) Closer virus—host interface look is shown, represented by the spike receptor-binding domain (RBD, in cyan) and the ACE2 peptidase domain (PD, in light gray). The residues of ACE2-PD interfacing with spike-RBD (in green) are also shown, which were used as one designed peptide with the aim to inhibit the virus—cell recognition schemed in (C). Human ACE2-based peptides binding to spike-RBD of (D) SARS-CoV-1 and (E) SARS-CoV-2 with the spike receptor-binding motif (RBM) is shown in red. The residue sequences of each extracted ACE2 peptide are presented in green in (D) and (E): α_1-helix composed of residues 22—44, 22—57, and residues 22—44 of α_1 connect by one glycine (G) with the loop region numbering from 351 to 357; inhibitors **1**, **2**, and **3** for sort.

Theoretical models serve as a powerful predictive approach in aiding the design of new treatments to block viral infection.[10] In this sense, we propose that models with the foundation in the energy landscape theory might contribute to attack this problem. The energy landscape theory was initially developed to study protein folding[11−14] and it has been a valuable framework in revealing many biological mechanisms related to folding and many other biomolecular functions, such as functional conformation dynamics, domain swapping, and binding mechanisms.[15−24] The structural formation of biomolecules has been described in this framework as a complex process that takes place in a multidimensional configurational space.[25] Folding, binding, and conformational rearrangements are depicted in terms of diffusion of configurational search down a funnel-like energy landscape, in direction to the minimum energy structure.[26,27] Also, natural protein sequences with funnel-like landscapes have energetic roughness that is relatively small compared to the global native state and the funnel slope is steep enough to overcome the local traps imposed by the roughness so that the biological function occurs.[11]

Biological function is controlled by the association of biomolecules, an essential event for cellular signaling and communication. Understanding the mechanisms involved in

molecular recognition processes and the correspondent proteins' roles are key targets for therapeutic interventions.[28] The classical binding mechanism called "lock-and-key" treats two binding biomolecules as rigid entities in their docking process.[29] Proteins are rather flexible, involving conformational changes; therefore, two other coupling mechanisms can be proposed. One is the "conformational selection", where a conformational change of one binding partner occurs before binding to the other. The second is the "induced-fit", where the conformational change occurs after binding.[30] These two flexible mechanisms are reasonable for small molecules that dock to proteins on a time-scale faster than the protein conformational change. However, this time-scale separation is not always clear for protein—protein or protein—peptide binding, which is induced during folding events of at least one of the involved biomolecules.[31,32]

The "binding-induced folding" association mechanisms can be cooperative—"*coupled* binding—folding" or noncooperative—"binding *prior* folding" and "binding *after* folding".[32] These binding—folding scenarios have been more investigated in the association of intrinsically disordered proteins (IDPs) in which their global conformational change (or folding) is always associated with their partners.[33] The coupling kinetics of binding and folding has been studied by experiments,
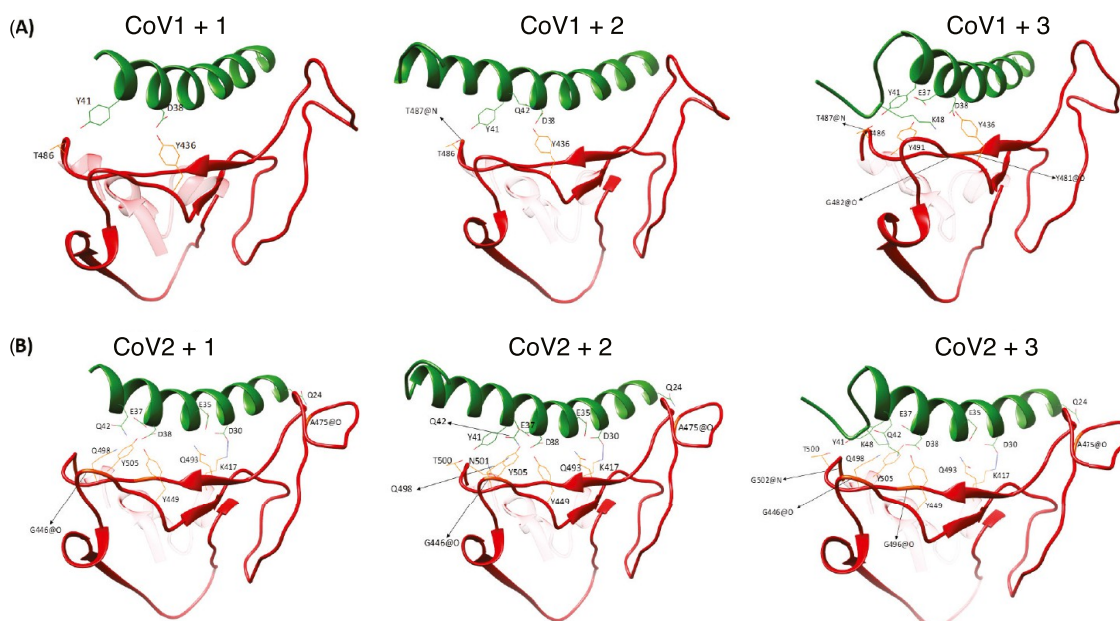
Figure 2. Hydrogen bonds formed by (A) SARS-CoV-1 (CoV1) and (B) SARS-CoV-2 (CoV2) and the inhibitors **1**, **2**, and **3**. Only the side chains of residues involved in hydrogen bonds are evidenced, and the hydrogen bond formed by the residue K417 (CoV2) and D30 of the inhibitors is highlighted in dark blue.

demonstrating a broad range of binding−folding scenarios.[34−47]

In this manuscript, natural and designed peptide binders known for having inhibitory action against coronavirus were selected by blocking the binding of spike-RBD to ACE2-PD (Figure 1C). Spike protein/gene is the preferred target site in SARS/MERS vaccine development, with many patents already deposited.[48] The objective is to determine the structural binding mechanisms and affinities of inhibitory peptides by characterizing their thermodynamic and kinetic profiles. This strategy could save lab work by computationally selecting new designs of peptides with a stronger affinity to SARS-CoV-2 than SARS-CoV-1. Also, virus surveillance will take place after the first generation of vaccines and drugs and there will be a continuous search for upgrades. Thus, new tools that are computationally less expensive can come in hand to select potential candidates to inhibit viral entry into human cells. At the beginning of the COVID-19 outbreak, many studies were performed to understand the structural aspects of the interaction between the virus and potential inhibitors and antibodies of spike-mediated infection[4,49−60] in a manner similar to the first SARS-CoV epidemic.[61−66] However, the dynamic aspects must be taken into account when designing new biomolecules,[4,66−69] and traditional molecular dynamics might be computationally expensive to screen a combinatorial variation of even small peptides, yet efficient to energy-minimized designed structures.[67,68,70−75] In this perspective, here we present a relatively low demand protocol to computationally characterize the difference in the binding thermodynamics and mechanisms of the peptides designed to inhibit the surface spike proteins of the old and new coronaviruses. The protocol is based on structure-based model (SBM) simulations, which has its foundation in the energy landscape theory,[76] already applied to study the spike prefusion dynamics.[77]

RESULTS AND DISCUSSION

Selected Peptide Inhibitors have Increased Hydrogen Bonds. The spike protein located on the surface of the coronavirus binds to the cellular receptor ACE2 of the host to deliver the virus genetic code.[78] Peptide binders are suitable therapeutics to interrupt the spike/ACE2 interaction by specifically binding to the interface region spike-RBD/ACE2-PD, preventing human infection.[79−82] Also, synthetic small biomolecules, such as aptamers of nucleic acid, bioconjugates of peptides, and polysaccharides, have been studied as protein blockers for coronavirus and other virus-related diseases.[56,83−87] Reports have shown that viral spike protein subunit vaccines produced higher neutralizing antibody titers and more complete protection than live-attenuated SARS-CoV-1, full-length spike protein, and DNA-based spike protein vaccines.[48] Protein vaccines targeting spike-RBD account for half of the vaccine patents.

Nanotechnology-enabled approaches like nanoparticles conjugated with the protein blockers enhance specificity/efficiency when used as delivery systems to inactivate SARS-CoV-2 in patients.[88,89] The computational design of peptides can contribute as an important step for speeding up nanomedicine-based approaches for COVID-19,[55,68,71−73,90−93] and characterizing their dynamics is a natural next step for the selection of potential candidates. For these reasons, combining *in silico* with experimental analyses narrows the large possible candidates among thousands of pharmaceutically active substances to be later employed in clinical trials.[88]

Three peptides constructed from the N-terminal amino acid residues of ACE2-PD were selected: two natural segments of α_1-helix (residues 22−44 and 22−57) and another peptide comprised of α_1-helix (residues 22−44) linked by a glycine (G) with the loop segment 351−357; hereafter coined as peptide inhibitors **1**, **2**, and **3**, respectively. The two natural peptides **1** and **2** exhibited a modest antiviral activity for SARS-CoV-1 RBD to human ACE2 with IC$_{50}$ of about 50 and 6 μM,

respectively, implying that **2** had a stronger affinity to RBD.[94] The artificial peptide **3** exhibited an even more potent antiviral activity of about 0.1 μM, implying that it had a much stronger binding affinity for SARS-CoV-1 than peptides **1** and **2**. Related to the novel coronavirus, it was reported that the natural fragment composed of residues 21−43 of the same human ACE2 α_1-helix can strongly bind to SARS-CoV-2 RBD with a micromolar affinity (dissociation constant, K_D = 1.3 μM)[68] that is comparable to the full-length ACE2 binding to SARS-CoV-2 RBD.[4] It was hypothesized by Huang et al. that the artificial peptide **3** may also bind stronger than peptide 21−43 (similar to peptide **1**) due to the high similarity among SARS-CoV-1 and 2 RBD interfaces with ACE2-PD[55] (Figures S1 and S2).

Peptides **1** and **2** binding modes with SARS-CoV-1 and 2 RBDs were constructed from the complex structures deposited in the Protein Data Bank to be used in this work (PDB codes 2ajf[61] and 6m0j,[51] respectively). Peptide **3** bound to SARS-CoV-2 RBD was obtained from the computational design of Huang et al.,[55] and CoV1+**3** was prepared by superposition to the CoV2+**3** and to the full-length ACE2-PD, followed by local energy minimization. Figure 2 shows the structures of the peptides bound to the spike-RBMs, representing the protein−peptide binding simulations of this study. Also, the sequence alignment of both spike-RBDs is presented in Figure S1, where the high similarity of the sequences is evident. Figure S1 also shows the sequence similarity among the three peptide inhibitors, residue binding contacts, and secondary structures.

Interfaces and interactions formed by SARS-CoV-1/SARS-CoV-2 and the inhibitors were analyzed using the protein interfaces, surfaces, and assemblies (PISA) server of the European Bioinformatics Institute (EBI), which predicts the most likely interfaces, based on size and energetic considerations.[95] Analysis of the complex's interfaces shows that SARS-CoV-1 and inhibitor **1** form a weak complex with only two hydrogen bonds (Y41/T486 and D38/Y436). This result agrees with our MD simulations, where the complex SARS-CoV-1 + **1** shows high flexibility. Nevertheless, Figure 2A shows that the addition of extra amino acids increases the binding efficiency of the inhibitors **2** and **3** toward the SARS-CoV-1 spike protein. The addition of 13 amino acids leads to the appearance of three extra hydrogen bonds in the SARS-CoV-1 + **2** complex (2 × Q42/Y436 and T487/Y41). Intriguingly, the inhibitor formed by the synthetic peptide of ACE2 boosted the number of hydrogen bonds to 7 (T41/Y486, K353/Y481, K353/G482, K353/G488, E37/Y491, and D38/Y436). It may be recalled that the majority of these interactions are also present in the crystallographic structure of the complex formed by SARS-CoV-1-RBD/ACE2.[54] It is worth mentioning that our analysis is in agreement with the experiments performed by Han and col., where increasing the size of the peptide caused an increase in the hydrogen bonds.[94] Examination of Figure 2B indicates that SARS-CoV-2 binds all of the inhibitors with a higher number of hydrogen bonds than SARS-CoV-1. Furthermore, inhibitors **1** and **2** showed a similar interaction mode toward the RBD-ACE2 domain, presenting 9 hydrogen bonds (Q24/A475, Q42/Y449, Q42/G446, D30/K417, E35/Q493, E37/Y505, D38/Y449, D38/Q498, and D38/Y449) and a salt bridge formed by residues D30 and K417. Here, it is important to highlight the hydrogen bond and salt bridge formed by residues D30 and K417, which have been featured as one of the most important for the affinity improvement of the viral protein toward human ACE2.[54]

Similar to SARS-CoV-1, the number of hydrogen bonds suggests that the synthetic peptide binds the SARS-CoV-2 protein with the highest number of hydrogen bonds (Figure 2B, right corner). The PISA web server identified 13 hydrogen bonds in the interface of the complex SARS-CoV-2 + **3** (Q24/A475, Y41/T500, Y41/N501, Q42/G446, Q42/Y449, D30/K417, E35/Q493, E37/Y505, D38/Q498, D38/Y449, K353/Q498, K353/G498, and K353/G502) and a salt bridge formed by D30 and K417, suggesting that sequence **3** might form the most stable complex and the most efficient inhibitor among the three sequences studied here. The designed **3** binding sites overlap with the binding sites of the *de novo* miniprotein inhibitors that showed picomolar to nanomolar affinity and blocked SARS-CoV-2 infection.[82]

Local frustration in the structures of SARS-CoV-1 and 2 complexed with the inhibitors **1**, **2**, and **3** was recognized using the Frustratometer Web Server.[96,97] Mutational and configurational frustration indexes were calculated for each molecular complex. Table 1 shows the percentage of minimally, neutral,

Table 1. Percentage of Minimally, Neutral, and Highly Mutational and Configurational Frustration Indexes of Interface Contacts between SARS-CoV-1 and 2 and the Inhibitors 1, 2, and 3

	mutational index			
protein	minimally	neutral	highly	total
CoV1+**1**	11 (26.2%)	18 (42.9%)	13 (31.0%)	42 (100%)
CoV2+**1**	7 (13.0%)	33 (61.1%)	14 (25.9%)	54 (100%)
CoV1+**2**	14 (29.2%)	21 (43.8%)	13 (27.1%)	48 (100%)
CoV2+**2**	11 (18.6%)	34 (57.6%)	14 (23.7%)	59 (100%)
CoV1+**3**	13 (16.5%)	49 (62.0%)	17 (21.5%)	79 (100%)
CoV2+**3**	12 (14.3%)	60 (71.4%)	12 (14.3%)	84 (100%)
	configurational index			
protein	minimally	neutral	highly	total
CoV1+**1**	7 (16.7%)	28 (66.7%)	7 (16.7%)	42 (100%)
CoV2+**1**	11 (20.4%)	39 (72.2%)	4 (7.4%)	54 (100%)
CoV1+**2**	9 (18.8%)	33 (68.8%)	6 (12.5%)	48 (100%)
CoV2+**2**	15 (25.4%)	39 (66.1%)	5 (8.5%)	59 (100%)
CoV1+**3**	15 (19.0%)	60 (75.9%)	4 (5.1%)	79 (100%)
CoV2+**3**	20 (23.8%)	61 (72.6%)	3 (3.6%)	84 (100%)

and highly frustrated interface contacts between SARS-CoV-1 and 2 and the inhibitors **1**, **2**, and **3**. The complexes formed by SARS-CoV-1 and 2 with the inhibitor **3** presented a high increase in the number of interface contacts when compared to the inhibitor **1**. A slight increase could also be seen in the number of interface contacts from the complexes formed by SARS-CoV-1 and 2 with the inhibitor **2**. Furthermore, a lower percentage of the interface contacts between SARS-CoV-1 and 2 (specially SARS-CoV-2) and the inhibitor **3** was inclined to be highly frustrated, unfavorable, in comparison with the other complexes (see Figures S3 and S4).

Designed Peptide Folds via Two-State Mechanism after Binding to Spike-RBDs. Protein folding and binding are intertwined processes closely connected to the cellular function. Both processes are similar at the thermodynamic level: the dynamics are mapped as diffusion over an ensemble of partially structured states, accompanied by a simultaneous reduction of the configurational entropy and the free energy due to solvent exclusion, hydrogen bonds, and salt bridge formations.[98] In addition, folding/binding kinetics are influenced by the thermodynamic free-energy barrier that
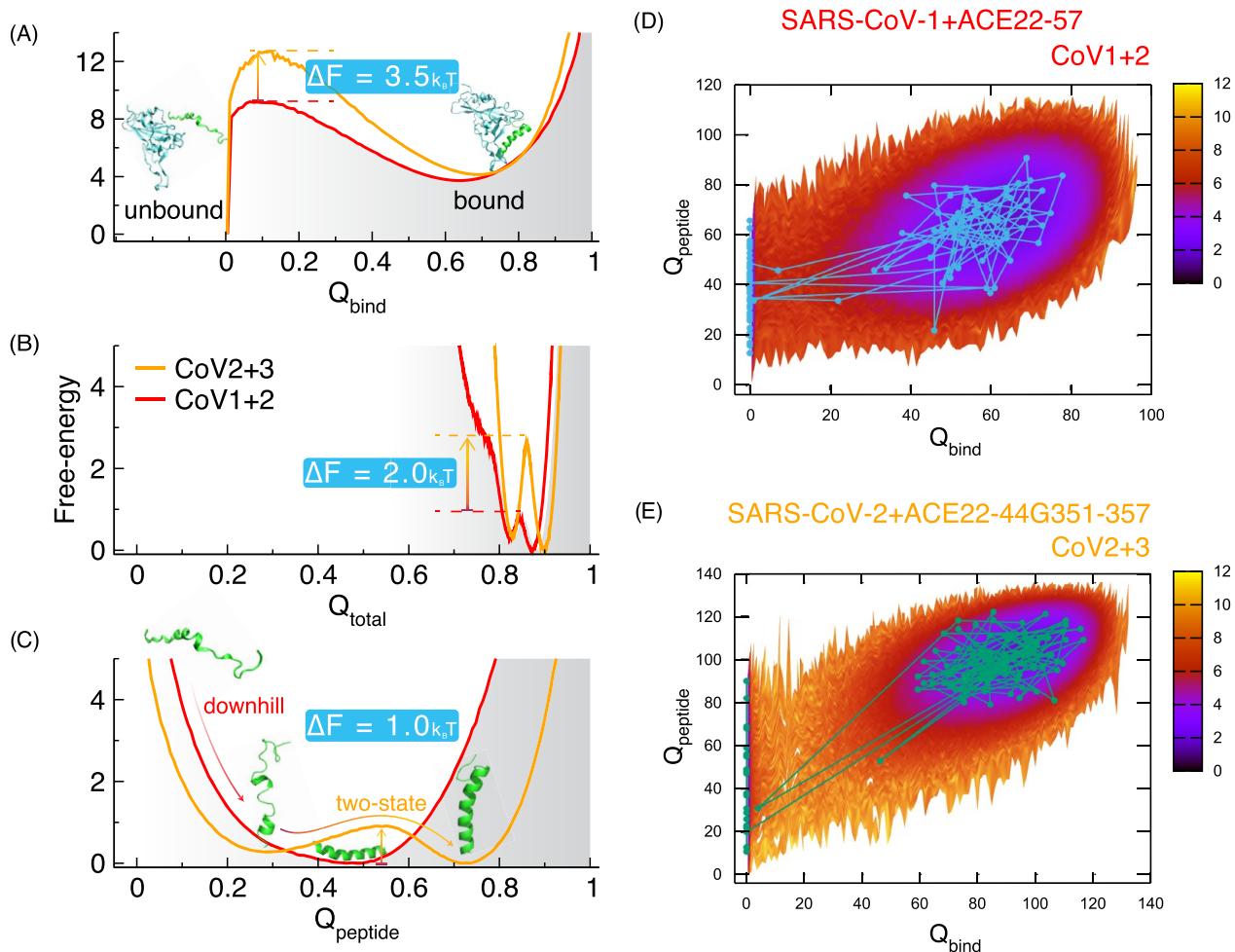
Figure 3. Free energy (F) of simulated ACE2 peptide binding to SARS-CoV-1 (red) and SARS-CoV-2 (orange) spike-RBD proteins. One-dimensional F profiles are shown as a function of reaction coordinates: a fraction of native (A) peptide–protein chain interface contacts (Q_{bind}), (B) inter plus intrachain contacts (Q_{total}), and (C) peptide contacts ($Q_{peptide}$). (D, E) show two-dimensional F profiles as a function of native contacts Q_{bind} and $Q_{peptide}$. In (A), the designed peptide ACE22-44G351-357 (inhibitor **3**) binds to the SARS-CoV-2 protein with a higher F barrier when compared with the α_1-helix peptide ACE22-57 (peptide **2**) binding to the SARS-CoV-1 spike domain. (C) shows that fragment **3** folds through a two-state mechanism upon binding to SARS-CoV-2 RBD, in contrast to a one-state (downhill) folding mechanism of **2** binding to the CoV1 surface. In addition, the coupled binding–folding processes are more cooperative to the designed **3** (E) than the natural **2** (D), despite the fact that the crossing barrier for **3** is higher and bumpier. F profiles are in units of $k_B T_{bind}$, with T_{bind} being the respective system's binding temperature.

separates the unfolded/unbound and the folded/bound states.[99] The thermodynamic barriers for the real proteins were reasonably described by SBMs in the α-carbon (C_α) representation of the protein.[100,101] However, side-chain packing can play an important role in the native contact interactions presented in the transition state of coupled protein folding and binding reaction,[37] and this can be achieved computationally when all atoms (except nonpolar hydrogen) are included in the pure C_α-SBM.[102,103] In either C_α and all-atom cases, and whether or not it is a Gō-model, protein topology and native contacts determine binding mechanisms in coupled binding–folding that are reflected by funneled energy landscapes, even if intermediates occur.[100,103−105]

The folding process of the selected peptides, coupled to the binding on the SARS-CoV-1 and 2 spike protein RBDs (CoV1 and CoV2, respectively), was simulated to characterize their thermodynamic quantities. The SBM, with all heavy (non-hydrogen) atom representation, was chosen to represent the system topology with default parameters. Figure S5A shows the residue contact map of three out of six simulated protein dimer

interfaces CoV1+**2**, CoV2+**1**, and CoV2+**3**, showing just the intermolecular contacts between two chains in the native structure defined as Q_{bind}. For each dimer, the model also accounts for the number of intramolecular contacts of the spike-RBD (Q_{spike}) and the peptide ($Q_{peptide}$). Q_{total} is the sum of the intramolecular and intermolecular native contacts (Q_{spike}, $Q_{peptide}$, and Q_{bind}) of each protein–peptide simulated system.

The computational SBM implemented here does not have a direct connection with the real temperatures. However, differences between quantities extracted from the theoretical temperatures have been proved to be proportional to the experimental temperatures, such as the Φ-value analysis that is based on the free-energy variation or folding rates of mutant/wild-type proteins.[106] The SBM is a topology-based model; thus, it is assumed that slight variations on the reduced temperature around the vicinity of the $C_v(T)$ up/down shape do not abruptly change the dimerization mechanism. Also, as experimentalists choose the quantity half-maximal inhibitory concentration (IC$_{50}$) to compare different inhibitory assays, we

choose $T = T_{bind}$ as the temperature to compare all of the simulated dimers. T_{bind} was defined as the temperature where C_v is maximum for each system that separates the transition between the states on (bound, low temperatures) and off (unbound, high temperatures). At this temperature, bound/unbound states are maximally sampled and the computed statistical quantities are better estimated.

Each dimer presented a broad yet a defined peak in the specific heat curve as a function of temperature ($C_v(T)$ in Figure S5B), determined by the thermodynamic analysis of the full set of simulated runs. In general, protein−peptide dimers of CoV1 showed higher T_{bind} than the respective peptide binding and folding to CoV2, although they are comparable. Another thermodynamic result is related to the designed fragment **3** that showed a higher peak in C_v for both coronavirus spike proteins compared to the natural peptides. This could be related to the insertion of the coil region on the spike-RBMs in addition to the α-helix, which may increase the energy/temperature necessary for transition.

The thermodynamic analysis of the free-energy profiles (F) as a function of selected reaction coordinates at the binding transition temperature (T_{bind}) was also computed. To improve the manuscript clarity, analyses were focused on the comparison of one natural with the designed peptide in complex with CoV1 and CoV2 and CoV1+**2** and CoV2+**3**, respectively. The results of all of the six peptide complexes are presented in the Supporting Information section for the sake of completeness. Peptide **2**, the longest selected α-helix peptide, was chosen to be compared with fragment **3** and complexed with CoV1 and CoV2. Their implications can also be discussed along with the different coronavirus spike proteins. CoV1 and CoV2 are very similar protein homologues in the sequence and structure. Inhibitors **2** (natural peptide) and **3** (designed fragment) differ after residue Ser44 in the C-terminal portion of the human ACE2-based peptides (Figures S1 and S2).

Figure 3 shows F as a function of reaction coordinates based on native contacts (Qs) for the selected protein−inhibitor dimers CoV1+**2** and CoV2+**3**. F as a function of Qs and position-based reaction coordinates radius of gyration (R_g), root-mean-square deviation (rmsd), and distance between the center of mass of the chains (d) for all of the simulated protein dimers are presented in Figure S6 for completion. The defined fraction of native binding contacts (Q_{bind}) was monitored for the coronavirus spike protein dimers, and the two-state on/off free-energy profiles are shown in Figure 3A for CoV1+**2** and CoV2+**3** and in Figure S6E for all dimers at T_{bind}. A broad bound state (around $Q_{bind} = 0.7$) is separated from a sharp unbound state (at $Q_{bind} = 0$) by an F barrier around $Q_{bind} = 0.1$. The natural peptide complex CoV1+**2** presented the lowest binding F barrier in Q_{bind} of around $9k_BT$ compared with the other complexes that resulted in a barrier between 12 to $15k_BT$. The peptides complexed with CoV2 presented, on average, a slightly higher binding $F(Q_{bind})$ barrier in relation to the CoV1 complexes. The same is also true for F profiles as a function of Q_{total} (Figure 3B), $Q_{peptide}$ (Figure 3C), and the position-based reaction coordinates (Figure S6, right panels). In Figure 3B, the majority of the native contacts of Q_{total} are related to the spike-RBDs (Q_{spike}), over 1600, in contrast to the total number of binding contacts of the two chains and the intramolecular contacts of the peptides (Q_{bind} and $Q_{peptide}$, respectively), both in the order of 100. Thus, in Figure 3B, Q_{spike} is oscillating in its folded state and this is the reason why the bound−unbound behavior is presented for values higher than $Q_{total} = 0.8$. The

two states of F in Figure 3B contain the unbound/unfolded state of the peptide on the left well and the bound/folded state on the right well, representing that dimer association and peptide/spike folding occur without distinction, in contrast to Figure 3A,C, where binding and folding are dissociated by the coordinates. Higher F barriers for the dimers were found along with the reaction coordinate Q_{bind} ($9-15k_BT$), suggesting that over one-dimensional landscapes, the rate-limiting step in RBD-peptide dimerization is the formation of native binding contacts among the chains interface at the transition state of this coordinate. The dimerization rate limit is followed by the position-based coordinates ($4-12k_BT$ in Figure S6).

It is interesting to observe in Figures 3C and S6A that during the dimerization processes, two distinct folding scenarios emerged for the peptides over F along their one-dimensional folding reaction coordinate: one-state (downhill) and two-state peptide folding mechanisms. It can be observed that natural peptides fold via a completely downhill scenario, i.e., there is no thermodynamic barrier in $F(Q_{peptide})$. The natural peptides **1** and **2** manifested a downhill-like mechanism as they bind to CoV1 and CoV2, except for CoV2+**1** that showed a small signal of two-state behavior in the coupled folding−binding two-dimensional landscapes, discussed in the next section. The downhill-like switches to a two-state folding scenario as the joined peptide **3** binds to CoV1 and CoV2 RBDs (Figure S7A) with a folding barrier of $1-2k_BT$ at the raised transition state ($Q_{peptide} \approx 0.5$) between the unfolded ($Q_{peptide} \approx 0.3$) and folded ($Q_{peptide} \approx 0.7$) states. Insertion of the loop sequence G351−357 on the natural peptide **1** to form the designed **3** created many additional inter and intrachain contacts (see Figure S5A), which may lead to this two-state folder. Enlarging the natural peptide from residues 22−44 to 22−57 only increases the size of the α-helix peptide and did not substantially increase the binding native contacts of the dimers as the addition of loop G351−357 (Figure S5A) did, and this could be one of the reasons of this change in the folding scenario. Another possibility could be that the information of peptide folding might not only be on the peptide sequence but also templated on the sequence of the binding partner as coupling proceeds,[107] although the partner sequence changes from SARS-CoV-1 to SARS-CoV-2 spike-RBD without affecting protein topology. This is a common feature of IDPs, and a large fraction of proteins undergo a disorder-to-order transition when recognized (templated) by their physiological partners.[107] However, some IDPs have their folding−binding pathways encoded within their sequence and are not templated by partner proteins with the same topology.[108]

The one-dimensional F profiles in Q_{bind} and $Q_{peptide}$ were combined to produce the higher two-dimensional F for the dimers CoV1+**2** and CoV2+**3**, shown in Figure 3D,E, respectively. $F(Q_{bind}, Q_{peptide})$ represents the coupled binding−folding pathways that a given dimer causes during the experiments. As shown in Figure 3D,E, projections over these two-dimensions also raised one thermodynamic barrier (transition state) for each dimer dynamics, with CoV2+**3** having a higher and rougher energetic barrier than CoV1+**2**. The recovered energetic barriers were on the same order of magnitude as the one-dimensional F barrier in Q_{bind}. In addition, the one- and two-state folding aspects of the two peptides are presented in the $F(Q_{bind}, Q_{peptide})$ projection on Q_{bind}. In Figure 3D, the downhill-folder natural peptide binds and folds almost without distinction of the coupled dynamics.
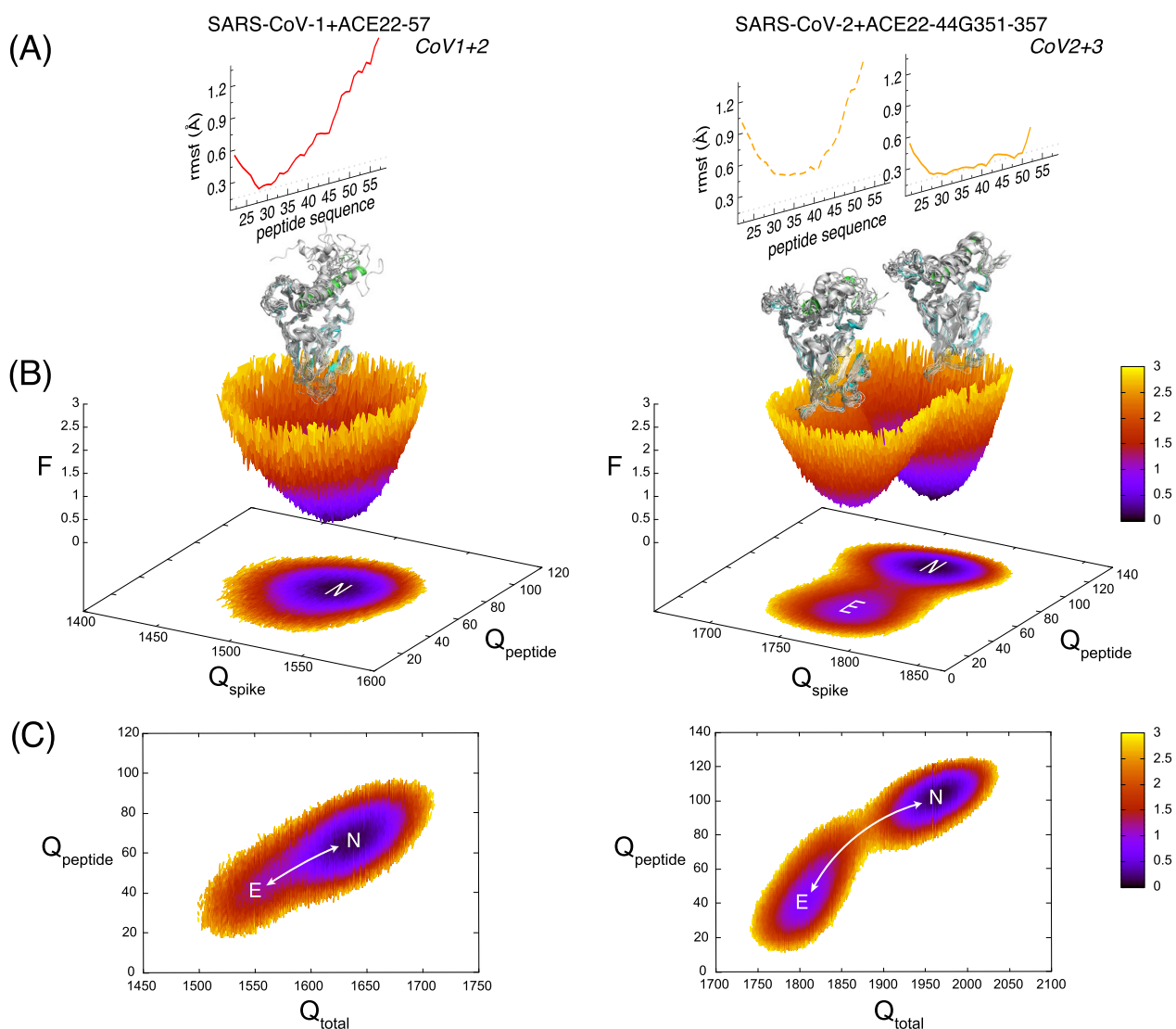
Figure 4. Two-dimensional free energy (F) of ACE2 peptides binding to the SARS-CoV-1 (left panel) and the SARS-CoV-2 (right panel) spike proteins. (A) Root-mean-square fluctuation (rmsf) of the peptides in the native (N) state. In the right panel, the rmsf for the designed peptide in the encounter complex (E) state is also shown (dash line). Representative simulated structures in these states (gray) are aligned with the native dimer structure (colored). F profiles are shown as a function of reaction coordinates of the native (B) peptide ($Q_{peptide}$) and protein (Q_{spike}) contacts and (C) inter plus intramolecular contacts (Q_{total}) and $Q_{peptide}$. The designed peptide ACE22-44G351−357 (inhibitor **3**) folds via a two-state mechanism (monitored by $Q_{peptide}$) upon binding to the SARS-CoV-2 RBD, which is oscillating in the protein native state (monitored by Q_{spike}); in contrast to a downhill folding mechanism of ACE22-57 (inhibitor **2**) binding to the SARS-CoV-1 protein. Also, the rmsf of CoV1+**2** is higher than CoV2+**3**. F profiles are in units of $k_B T_{bind}$, with T_{bind} being the respective system binding temperature.

In contrast, Figure 3E shows that fragment **3** binds to spike after folding, recovering a two-state kind of coupled mechanism. **3** binding−folding pathways are more cooperative, although there is a higher and funneled energetic barrier to cross. Once bound, the natural peptide can fold and unfold more freely than the fragment, an aspect that will be thoroughly discussed in the next section. Highly dynamic "fuzzy" complexes, indicating a malleable binding−folding pathway, were previously reported for IDPs complexed with stable proteins by the experiments temperature-jump[22] and multinuclear relaxation dispersion NMR.[40] For another IDP-protein dimer, it was reported that a free-energy barrier shows up separating the self-assembly process.[104]

Two-State Designed Peptide is Less Flexible on the Spike-RBMs. The coupled dynamics of peptide folding and binding to spike-RBD was investigated by analyzing two-dimensional free-energy profiles. The binding was captured as the one-dimensional $F(Q_{bind})$, as shown in Figure 3A. Folding was captured by $Q_{peptide}$ in Figure 3C. The composition of Q_{bind} and $Q_{peptide}$ to form a two-dimensional F resulted in a landscape with a not so clear valley at the unbound state since this state has 0 intersubunit contacts (Figure 3A), resulting in a sharp valley located at the boundary of Figure 3 (right panel, not clear to inspect) and another broad valley at the center, as previously described in many works.[21,103] After combining all of the analyzed reaction coordinates of Figure S6, it was found that the combinations presented in Figures 4, S7, and S8 presented two broader valleys at the bound and unbound states. These combinations enabled more binding−folding mechanism analyses in the course of the sampled states.

Figure 4 shows two-dimensional free-energy landscapes for the two protein−peptide dimers CoV1+**2** and CoV2+**3** at the

defined transition temperature, T_{bind}. Figure 4B presents F as a function of the reaction coordinates $Q_{peptide}$ and Q_{spike}, clearly displaying one valley for CoV1+**2** and two wells for CoV2+**3**. Projection of F in Q_{spike} (Figure S6C) shows one defined valley in F for both systems with the fluctuations and sampling along Q_{spike} of the protein monomer being more rigid in CoV2. This is confirmed by the root-mean-square fluctuation (rmsf) analyses of the simulated protein dimers in Figure S10. Figure S10 shows the rmsf of each residue, according to the primary structure of CoV1/CoV2 proteins and the ACE2-based peptides. Interestingly, the overall flexibility of the complex CoV1-**2** is the highest compared to the complexes formed by CoV1 with inhibitors **1** and **3** and the three CoV2 dimers. These differences are even more evident in Figure S10D, where the rmsfs are incorporated in the complex structure as tube radius. The binding of the three inhibitors **1**, **2**, and **3** makes the overall structure of CoV2 spike-RBD less flexible, which is an indication of a tighter binding toward the novel coronavirus protein. In addition, peptide fluctuations are higher in CoV1 than in CoV2, as represented by the peptide rmsfs in Figures 4A and S10. This rigidity of the SARS-CoV-2 spike receptor-binding motif has already been reported by simulations and experiments, and it was hypothesized as one of the reasons for its enhanced infectivity.[59,60,67,74]

In Figure 4B, it is the projection of F in $Q_{peptide}$ that differentiates the one-to-two wells in $F(Q_{spike}, Q_{peptide})$ landscapes between the two dimers. The downhill and two-state folding mechanisms of the peptides along the $Q_{peptide}$ coordinate are again evident for CoV1+**2** and CoV2+**3**, respectively. For the two-state fragment folder in CoV2+**3**, there is an F barrier separating the two valleys on the order of $2k_{B}T$, which is the double of the free-energy barrier of the one-dimensional $F(Q_{peptide})$ (Figure 3C). In this high order projection of F in Figure 4B, conformational rearrangements of the spike protein along Q_{spike} are also taken into account combined with folding in $Q_{peptide}$ to overcome the barrier. Figure 4 shows one valley marked with the letter "N" standing for the "Native" state in which both protein and peptide are folded and bound. "E" denotes the "Encounter" complex state in which the dimer can be partially bound or unbound, the protein can be folded yet slightly loose and open, and the peptide is unfolded but partially structured (Figure 4A). This two-state dimerization mechanism emerges due to the temperature selected to plot $F(T_{bind})$ that samples these mentioned states without separating them in the classic three or more dimerization states reported for bigger dimers.[21,103] C_{v} has a wide peak around T_{bind} in Figure S5B, suggesting a smooth transition where these states coexist. The completely unbound and unfolded state for the peptide was seen in higher simulated temperature data. Peptides are small compared with spike-RBDs, and the peptide dynamics are faster in sampling states at T_{bind} as shown in a small part of the representative time trajectory in Figure S7B,C. Dimers of CoV2 with natural peptides **1** and **2** also presented this two-state dimerization profiles in $F(Q_{spike}, Q_{peptide})$, however, with lower barrier and elevated E well minima comparing with N valleys (Figure S9A). The existence of more than two states at the $C_{v}(T_{bind})$ peak does not guarantee that these wells will have the same depth in Figures 4, S8, and S9 at T_{bind}.

Figure 4C presents $F(Q_{total}, Q_{peptide})$ landscapes at T_{bind} for CoV1+**2** and CoV2+**3** with one and two global wells, respectively. Q_{total} contains Q_{spike}, despite being the largest amount of native contacts, and its value fluctuates around a narrow valley where spike-RBD is folded (Q_{spike} minimum in Figure S6C). Q_{total} also contains Q_{bind} and $Q_{peptide}$, and these reaction coordinates have a smooth change in F at the transition temperature T_{bind} (for example, Figures S6E and S7A, respectively). Apart from $Q_{peptide}$ that monitors the peptide folding mechanism separately, as shown in Figure 4C, we would say that the increase in Q_{total} is proportional to the increase in Q_{bind}, representing the minimal path of the diagonal. With that being stated, the CoV1 dimer increases Q_{total} concomitantly with the increase in $Q_{peptide}$, suggesting a mechanism that binding and folding of the peptide occurs concomitantly in Figure 4C. The E state is marked in Figure 4C as a reference for the discussion of the coupled binding—folding mechanism of the CoV1 dimer, although it is not a deep minimum valley per se. Figure S7B shows that $Q_{peptide}$ changes in a manner similar to Q_{bind} during the selected few steps of CoV1+**2** molecular dynamics, again suggesting the peptide coupled binding—folding mechanism.

CoV2 dimer dynamics over $F(Q_{total}, Q_{peptide})$ shows a different minimal path diverging from the diagonal that separates E and N states. The off-diagonal path suggests that the folding of the designed fragment **3** (same for the natural **1** in Figure S9B) is coupled to binding, yet slightly different from **2** with CoV1. The separation F barrier of about $1k_{B}T$ for the fragment folding is small compared to the thermal fluctuations that could also be around $k_{B}T$;[109] thus, it does not impose an obligatory step to the fragment being completely folded to bind to the monomer. Yet, it seems that the peptide should be partially structured in the native conformation, reflected by the first increase in $Q_{peptide}$, and then binding to CoV2 occurs, shown by the second increase in Q_{total}. The off-diagonal path suggests a mechanism of folding after binding, although folding occurs by crossing an energetic barrier. Figure S7C shows that $Q_{peptide}$ still changes around $Q_{peptide} = 0.3$ after the peptide is unbound at step 32, although Q_{bind} remains equal to zero, again suggesting the folding-upon-binding mechanism of the fragment. CoV2+**3** dimer forms after transposing the $F(Q_{total}, Q_{peptide})$ barrier of over $2k_{B}T$ that occurs after at least 30% of the designed native contacts being formed at T_{bind}.

It is important to emphasize that our findings indicate that the limiting rate for the dimer assembling of the two coronaviruses was the thermodynamic barrier on the one-dimensional Q_{bind} coordinate ($9-15k_{B}T$) and the energetic barrier along $Q_{peptide}$ that segregates one-to-two-state peptide folding; therefore, binding is the critical step. Figures S8C and S9C show the two-dimensional F of the simulated dimers as a function of the distance between the center of mass between the two chains ($d_{spike-peptide}$) and $Q_{peptide}$. $F(d_{spike-peptide}, Q_{peptide})$ shows an unbound (U) state in which the distance between the protein and the peptide is bigger than the native/bound (N) and the encounter (E) complex states, both located at almost the same $d_{spike-peptide} \approx 2$ nm. It can be observed that U are wide wells approximately aligned with the E state in which both have a low level of nativeness for the peptide, i.e., the peptide was found to be unfolded at U and E. Despite the fact that there is a difference between the two natural and the designed peptides en route to the N well. There is no barrier between E and N for the natural peptides; only the fragment has to overcome an energetic barrier to fold, even though the three peptides are limited by a free-energy barrier to reach the spike proteins at $d_{spike-peptide} \approx 2$ nm. Thus, this is an indication that the fragment has a more cooperative coupled binding—folding dynamics than the natural peptides. These two coupled
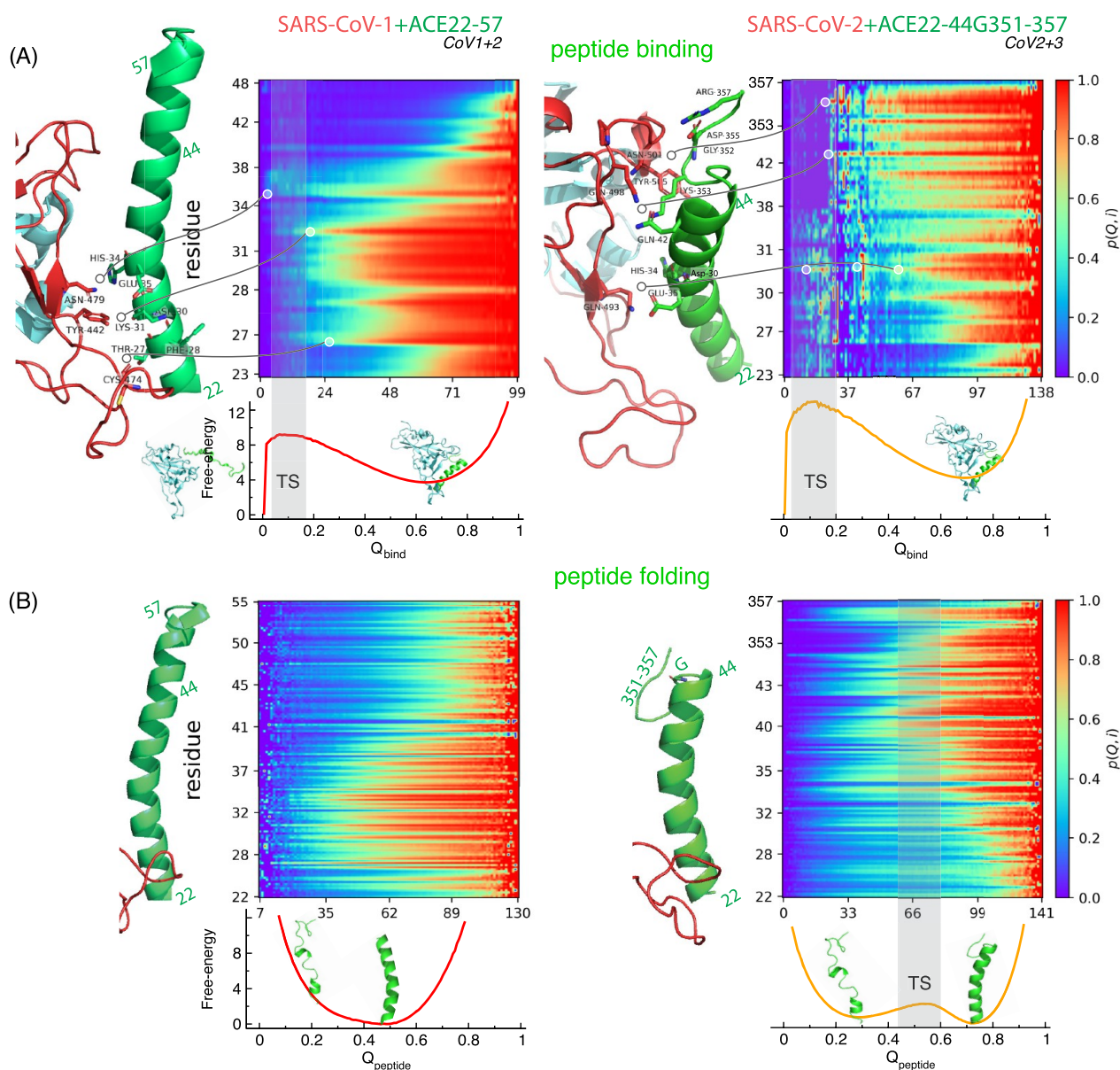
Figure 5. Contact formation probability as a function of (A) binding (Q_{bind}) and (B) peptide ($Q_{peptide}$) native contacts of each peptide atom i ($p(Q, i)$) for CoV1+**2** (left panel) and CoV2+**3** (right panel). The atom numbers were replaced by the respective residue number to a better visualization. The normalized contact probability increases from zero (blue) to 1 (red). Both cases were analyzed at the respective binding temperature T_{bind}. For each dimer, the free-energy profile (F/k_BT) as a function of (A) Q_{bind} and (B) $Q_{peptide}$ with the transition state (TS) area shaded in gray is also shown. Main native contact interactions involved in the early binding event are marked in the structures at the left side of each panel in (A). Peptide inhibitor **2** binds and folds to CoV1 by the N-terminal portion of its α-helix. Fragment **3** also attempts to bind to CoV2 by the N-terminal portion at the transition state (right panel in A); however, after crossing TS, **3** unbinds its N-terminal region and binds and folds via its C-terminal loop segment.

events determine the kinetics and the thermodynamics of the studied protein dimers and it is feasible to be characterized by all-atom SBM simulations.

Designed Peptide has Binding Contacts Tightend by the Secondary Loop Site. The structural evolution content of the folding-upon-binding mechanism of the spike-ACE2-based dimers was analyzed by building average contact formation probability maps. The probability map of an atom i to form native contacts along with a reaction coordinate Q was computed ($p(Q, i)$ given by eq S3). In this probability map, each pixel corresponds to the average frequency of an atom belonging to a residue to form their atom—atom native contacts in a specific point of the reaction coordinate. $p(Q, i)$ is

computed over a long time trajectory at a constant temperature run. The simulations contain about 1600 atoms belonging to the two chains of each protein—peptide dimer. Thus, it was convenient to show in the y-label the residue index instead of the original atom numbering, which produced irregularly distributed labels, yet, human-readable.

Figure 5 shows the probability map of the peptide atoms to form native contacts along the binding (Figure 5A) and folding (Figure 5B) reaction coordinates for the dimers CoV1+**2** (left panels) and CoV2+**3** (right panels), both at T_{bind}. Figure 5B also shows the free-energy profile for the binding coordinate ($F(Q_{bind})$), with the defined transition state (TS) region shaded as the gray area. In addition, the probability maps for

the three peptides simulated with SARS-CoV-1 and 2 spike-RBDs are presented in Figures S11 and S12, respectively. Q_{total} and Q_{spike} contain thousands of native contacts with similar probability maps, and this was the reason to show only $p(Q_{\text{spike}}, i)$ in Figures S11C and S12C. The spike protein is relatively well folded (red maps in Figures S11C and S12C) during the binding and folding contact formation of the peptides, which are on the order of a hundred. The peptides are α-helix-based and this linearity in their structure and sequence are reflected in the high similarity between the two portions of Q_{bind} probability maps of the proteins (top half) and peptides (bottom half) in Figures S11A and S12A.

At the unbound state (blue strip at $Q_{\text{bind}} = 0$ in Figures 5A, S11A, and S12A), the almost folded spike proteins approach the peptides that are completely unfolded and disordered, represented by the blue strip region at $Q_{\text{peptide}} = 0$ on the maps in Figures 5B, S11B, and S12B. The sharp transition to the bound state starts when there are between 4 and 10 binding native contacts formed for the peptides, which is the beginning of the TS in Figure 5A. At TS along Q_{bind}, many nonspecific protein−peptide contacts are formed with a probability of up to 50%, except for the constructed **3** that also showed some binding contacts made with a probability of above 80% at some positions in TS (red dots at TS on the maps). Many other protein−peptide native interface contacts start to be made with high probability in red as binding proceeds by crossing TS along Q_{bind}.

The natural peptides **1** and **2** have similar binding contacts being formed with the spike-RBMs (Figure S5A). Figure 5A shows that CoV1 first casts the natural peptide **2** by binding the protein residue Asn479 to the peptide residue Hist34 at $Q_{\text{bind}} \approx 0$, followed by Tyr442 binding to peptide residues Lys31 and Glu35. CoV1 proceeds by binding residues Asn473 and Cys474 to the peptide residues Thr27 and Phe28. These two interface regions are highly hydrophilic on both surfaces, protein and peptide, as is shown in Figure S13 (left panels). Natural peptide residues over Tyr41 do not contribute to binding significantly. Previous experiments showed that CoV1 residues Asn479 and Thr487 were associated with the recognition of the human ACE2 receptor in addition to residues Tyr442, Leu472, Asp479, and Asp480 that allowed interspecies infection.[110] Residue Thr487 is a CoV1 residue important for binding of the designed **3** loop segment, as shown in Figure S11A (right panel). The corresponding CoV1 residues Asn479 and Thr487 in CoV2 are the polar residues Gln493 and Asn501, respectively, in which they also play a key role in the ACE2 recognition by CoV2.[111]

The designed peptide **3** has a different sequence for the native binding contact formation revealed by the probability maps. Figure 5A shows that fragment **3** binds at the transition state to CoV2 by many interface contacts from its N-terminal portion attempting to follow the same sequence of events of the natural peptides. However, after crossing TS in the $F(Q_{\text{bind}})$ profile, **3** unbinds some of its N-terminal contacts and binds its C-terminal loop segment to CoV2. In Figure 5A, CoV2 binds to fragment **3** after TS by residue Asn501 to peptide residue Lys353, followed by Gly354, Asp355, and Arg357. CoV2 residues Gln498 to Tyr505 also contribute to these binding contacts to the loop segment. This is connected with the recent finding that, among the novel spike mutations, SARS-CoV-2 has the maximum van der Waals interaction between residues CoV2-Asp491 and ACE2-Lys353.[70] This partial interface formation proceeds by CoV2 residue Gln498

connecting to peptide residue Gln42. The loop segment of **3**, present in the wild-type ACE2-PD as a secondary binding site, creates many additional intermolecular native contacts with the spike-RBD tightening up the protein−peptide interaction.

Figure S13 shows how this partial interface, created by the turn residues Gln498, Pro499, and Asp501 of CoV2, is more hydrophilic than the similar (mutated) residues in CoV1 (Figures S1C and S2). Also, the Trp500 surroundings in CoV2 showed to be more hydrophobic than in the same position in CoV1, as is pointed by the upper orange arrow in Figure S13. In CoV1, the first probable binding residue was Asn479 that is mutated by Gln493, which maintained the hydrophilic nature of this site in both proteins. However, other mutations surrounding Gln493 in CoV2 created a more hydrophobic site than in CoV1. This increase in hydrophobicity caused by mutations on this CoV2 site could be another reason for the late capture of fragment **3** residues His34 and Glu35 during the binding process, despite the large number of binding attempts at TS. This observation suggests room for fragment **3** binding affinity improvement. These two mechanisms described by the natural and designed peptides are similar in CoV1 and CoV2 with a difference that many binding contacts were made earlier in CoV2 (Figure S12A) than in CoV1 (Figure S11A).

The peptide binding processes are accompanied by the folding of their linear structures, which can be seen in the probability maps. Figure 5B shows the probability of a peptide residue to form intramolecular native contacts at a specific position of the folding coordinate, Q_{peptide}. Figure 5B presents $p(Q_{\text{peptide}}, i)$ for dimers CoV1+**2** (left panel) and CoV2+**3** (right panel), both at T_{bind}, in addition to the probability maps of the three peptides simulated with SARS-CoV-1 and 2 spike-RBDs presented in Figures S11B and S12B, respectively. It was discussed in the previous sections by inspecting one- and two-dimensional F profiles that, upon binding, the natural peptides **1** and **2** fold via the downhill mechanism and the designed fragment folds via the two-state mechanism. These two folding mechanisms were again represented by $F(Q_{\text{peptide}})$ in Figure 5B, with the transition state shaded as the gray area only for the two-state-folder fragment. The probability maps of Q_{bind} resemble those of Q_{peptide} in Figures 5, S11, and S12. This is a signal that as a peptide atom/residue is captured (binding), on average, it assumes its native conformation (by folding) that is represented by the red pixels in Figure 5B.

An unstructured protein might have a greater capture radius for a specific binding site than the folded state with its restricted conformational freedom. Therefore, the unfolded state binds weakly, followed by folding, as the protein approaches the binding site, and the binding rate is enhanced. This scenario has been hypothesized over a couple of decades as the "fly-casting" mechanism and it has been studied by SBMs in which the thermodynamic barriers for the real proteins were reasonably described by the model in the α-carbon (C_{α}) and all-atom representations of proteins.[100−103] Thus, folding-upon-binding, similarly to the proposed fly-casting mechanism, might be one of the possible ways of interaction between the spike-RBDs and the peptides.

In Figure 5B, the α-helix peptide **2** starts the downhill folding (at $Q_{\text{peptide}} \approx 0.1$) by their N-terminal residues in a similar manner as the residues bind to CoV1, as discussed in Figure 5A. The downhill F profile has its minimum at $Q_{\text{peptide}} \approx 0.5$, meaning that around 50% of the peptide native contacts were not formed most of the time during the simulation at T_{bind}. The probability map of peptide **2** projected on F shows
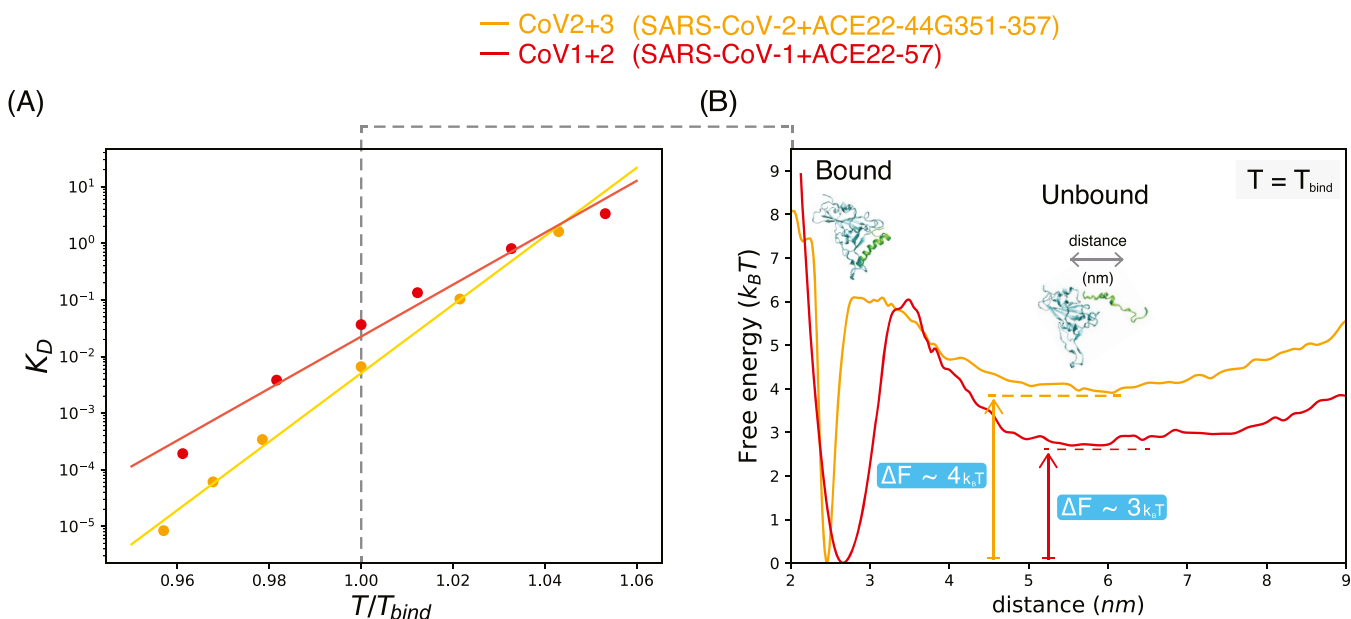
Figure 6. (A) Equilibrium dissociation constant (K_D) as a function of temperature for two simulated dimers: CoV1+**2** (red) and CoV2+**3** (orange). K_D was calculated using eq 1 (circles) and the line represents a simple linear fit to the data that helps to guide the eye. CoV2+**3** has lower dissociation constants for increasing T than CoV1+**2**, implying higher binding affinity in temperatures around T_{bind}. (B) Free energy (F) as a function of the distance between the center of mass of the protein and the peptide at T_{bind}. At $T = T_{bind}$ in (A), the CoV2+**3** equilibrium K_D is about one order of magnitude smaller than CoV1+**2**, which is a reflection of the higher ΔF stability between bound/unbound states in (B). Temperature is normalized by the respective dimer binding temperature (T/T_{bind}) and F profiles are in units of $k_B T_{bind}$.

that residues over Tyr41 are not yet formed at the free-energy lowest level, suggesting that the C-terminal region of the natural peptide is more flexible, unbound, and loose in CoV1. However, folding of the natural peptides in the presence of CoV2 starts in residues closer to the C-terminal domain, as shown in Figure S12B, in addition to the fact that they are less flexible than in CoV1. Figure 5B shows that the folding of fragment **3** in the presence of CoV2 also starts from its C-terminal loop residues that have many of their intramolecular native contacts formed at TS of $F(Q_{peptide})$. In addition, few **3** residues close to the N-terminal sequence are not formed at the folded state in $Q_{peptide} \approx 0.8$. Regarding **3** with CoV1, the peptide native contacts from the N-terminal residues are formed before TS, similar to the natural peptides shown in Figure S11B. Nevertheless, some contacts are unmade after TS and a less specific native contact formation proceeds as the folding occurs, also leaving some N-terminal residues unfolded at the folded well.

In general terms, the three peptides (**1**, **2**, and **3**) in a disordered state are cast (fly-casting) by the two spike-RBDs CoV1/CoV2 with the hydrophilic Asn479/Gln493 residues being the bait of the exposed hydrophilic region close to the peptide residue His34. This precise requirement of a small partner search diameter is necessary for the α-based peptides to dock into the protein binding site interface. The capping loop CoV1/CoV2 residues Thr487/Asn501 play an essential role in the association of the ACE2-based secondary binding site, the **3** loop region. The inserted loop residues of **3** increase the binding contacts in the two spike-RBDs, a major hydrophilic region. These polar contacts formed near the casting and the loop residues correlate with the hydrogen bonds formed between the proteins and the peptides. Figure 2 shows that CoV2 has more hydrogen bonds formed with the peptides than CoV1, which are the new hydrophilic contacts that emerged in CoV2 by residue mutations that occurred in

CoV1. It was reported by binding simulations of the full-length ACE2-RBD of SARS-CoV-1 and 2 that these differences in the hydrophobicity and hydrogen bond network of the two dimers govern the enhanced binding affinity of the novel coronavirus.[74] Also, polar residue mutations in SARS-CoV-2 result in a greater electrostatic complementarity than that of the SARS-CoV-1 complex,[74] although the simulated electrostatic and pH-dependent free-energy affinities of both dimers were similar.[112] It is suggested that this similar, yet enhanced, binding energy of the SARS-CoV-2 spike protein is not due to a single mutant but because of the sophisticated structural changes induced by all mutations together.[70] This has implications for antibody therapeutics and vaccines that might be effective in combating different SARS-CoV-2 isolates affected by common mutations.[113]

Peptide Binding Affinity is Higher for SARS-CoV-2 Spike-RBD. Association rates and binding affinity constants have been investigated extensively for interactions between proteins that can be folded or partially folded and for complexes where one or more partner is initially disordered.[114] Solvent and temperature dependence of the association rates indicate that kinetics of a coupled folding and binding reaction is limited by the free-energy barrier or transition state.[115] The experimentally observed binding process of the binding–folding reaction was consistent with molecular dynamics simulations of the coarse-grained C_α-SBM performed previously,[39] which was similar to the all-atom SBM simulations of this study. The molecular binding affinity is related to the equilibrium dissociation constant ($K_D = 1/K_A$) that measures the propensity of a dimer in reversibly separating its two components. Therefore, a low dissociation constant is related to higher biding affinity and vice-versa. One can measure K_D from the ratio between the kinetic dissociation (k_{off}) and association (k_{on}) rate constants ($K_D = k_{off}/k_{on}$).[39] From the thermodynamic point of view, K_D can also be

associated with the Gibbs free-energy change during the dissociation/binding events. The stability of a protein−ligand binding can be determined by the magnitude of the free-energy variation upon binding (ΔG) that is connected to K_D by[116]

$$\Delta G = k_B T \, \ln(K_D) \tag{1}$$

From the thermodynamic stability given by eq 1, it is possible to measure the equilibrium K_D and to infer the biomolecular binding affinity of the simulated protein−peptide dimers. The equilibrium dissociation constant was evaluated for a range of temperatures around T_{bind} using the Helmholtz free-energy stability (ΔF) in eq 1, which is obtained in the simulations by the Weighted Histogram Analysis Method (WHAM).[117] F was evaluated as a function of the distance (d) between the center of mass of the spike-RBDs and the peptides (Figure S6d), differing from the previous sections that analyzed F of native contact-based coordinates (Figure S6, left panels). We observed that the coordinate Q_{bind} is suitable for mapping the thermodynamics of the contact formation mechanism; however, Q_{bind} can give imprecise information about the association. For instance, one of the dimer's components could be slightly rotated from the native bound conformation resulting in a low Q_{bind}, but in a very close distance between the protein−ligand.

Figure 6A shows an increase of the equilibrium dissociation constant (K_D) with temperature for the dimers CoV1+2 and CoV2+3. At $T = T_{bind}$, Figure 6B presents the $F(d)$ profiles for CoV1+2 and CoV2+3 that resulted in the thermodynamic stabilities between the bound/unbound states of $\Delta F \sim 3k_B T$ and $\Delta F \sim 4k_B T$, respectively. This difference in ΔF between the two dimers at T_{bind} is mainly responsible for the difference of about one order of magnitude in K_D in Figure 6A. The dissociation constant of CoV2+3 is lower than the K_D of CoV1+2, implying that the binding affinity is higher. This trend is also observed for the other equilibrium K_D reported in Table 2, in which it predicts that the binding affinity of the three peptides with the novel spike-RBD CoV2 is higher than with SARS-CoV-1 RBD.

Table 2. Equilibrium Dissociation Constant (K_D) between the SARS-CoV-1 and 2 Spike-RBDs and the Peptide Inhibitors 1, 2, and 3, Evaluated at the Binding Temperature (T_{bind}) of Each Protein Dimer

spike-RBD + peptide	$K_D(T = T_{bind})$
CoV1+1	1.5×10^{-2}
CoV1+2	3.7×10^{-2}
CoV1+3	1.4×10^{-2}
CoV2+1	2.7×10^{-3}
CoV2+2	1.6×10^{-3}
CoV2+3	6.6×10^{-3}

The analysis of binding events can be a rather difficult task. It is strongly dependent on choosing the perfect setup and experimental conditions, and it is also advisable to measure binding interactions on multiple platforms for cross-validation. Two label-free binding measurement platforms are commonly used: the surface plasmon resonance (SPR) and biolayer interference (BLI).[118] These two platforms were recently employed by the experimentalists to analyze the binding of optimized ACE2-based peptides and antibodies targeting the full spike protein (or its RBD) of the novel coronavirus in which K_D ranged from picomolar to nanomolar affinities.[119]

The full ACE2 enzyme dissociation constant of the SARS-CoV-2 spike protein is reported to be on the higher end, the nanomolar binding affinity,[4] though that of SARS-CoV-1 were reported by different BLI experiments to be similar[50,120] or to have an up to 20-fold higher K_D,[4] meaning lowered affinity to CoV1. The *de novo* designed ACE2-based peptide and miniprotein affinities to CoV2 were also reported to have comparable or lower affinity to CoV1.[68,82,93,121−124] This is an indication that ACE2-derived peptides might be, in some cases, more sensitive to CoV2 than to CoV1, that is, qualitatively in line with the theoretical binding affinities estimated in Table 2. The natural peptides 1 and 2 and the designed 3 are based on the original sequence of the human ACE2 that is shown to be suboptimal for binding CoV2 in the nanomolar range. This opens the opportunity to redesign these peptides to significantly improve their binding affinity up to the picomolar range, inhibiting SARS-CoV-2 and its mutations from entering human cells and hindering its fast transmission.

■ CONCLUSIONS

Many cellular activities are determined by the recognition of at least two flexible biomolecules. In this manuscript, two sets of dimers relating to SARS-CoV-1 and 2 spike-RBDs were simulated (CoV1 and CoV2), in which each RBD was simulated with three peptide inhibitors of increasing sequence length based on the α_1-helix of ACE2-PD, two naturals (1 and 2) and one designed (3) by including a secondary loop sequence. The thermodynamic analysis showed that the three peptides have different binding and folding free-energy barriers in the presence of CoV1 and CoV2 and, for some coordinates, even a different transition state position. Kinetic analysis of binding/folding native contact formation also revealed different patterns between the two sets of dimers. In these two sets, the three peptides have the same residue sequence; therefore, the difference in the binding partner sequence seems to have an important role in the binding affinity and folding of the peptides. This difference in the binding−folding process of the binder that is templated by the protein partner was already reported for some IDPs;[107] however, it is not a universal feature.[108] In the case of the coronavirus dimers of this study, just folding by itself separated the natural and designed peptides into two classes of mechanisms; thus, the coupled binding-upon-folding mechanisms were dictated by both protein−inhibitor residue sequences.

Figure 7 summarizes the two binding−folding mechanisms of the studied protein−peptide dimers. Figure 7 shows that it starts with the conformational rearrangements of the superficially "open" spike-RBMs catching the peptides at the encounter complex step and then the binding occurs. The RBM surface accommodates the peptide at the same time that folding proceeds. This flexible binding−folding mechanism is more cooperative for the designed peptide, as shown in Figure 7B, due to the free-energy barrier for folding that 3 has to cross to reach the native/bound state (Figure 7A). Free-energy barriers for binding over the native contact-based and coordinate-based reaction coordinates were similar when comparing SARS-CoV-1 spike protein dimers with SARS-CoV-2, although CoV2 dimers resulted in increased energetic barriers. Our results are in alignment with recent computer simulations showing that electrostatic and van der Waals binding energies are similar, yet higher, for the SARS-CoV-2 spike protein bound to ACE2-based peptide inhibitors, full-length ACE2-PD, and monoclonal antibodies.[72,74,112] It is also
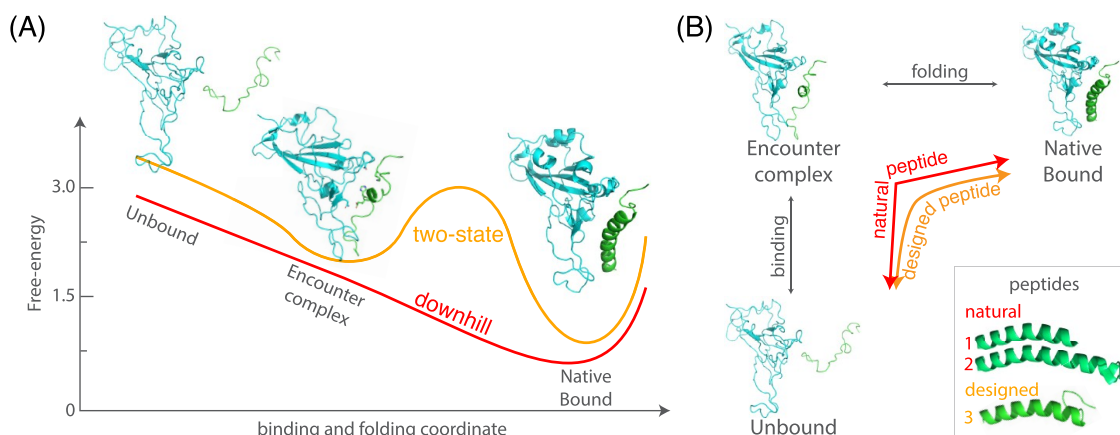
Figure 7. Scheme of the binding and folding dynamics of the studied dimers with the natural peptides **1** and **2** and the designed fragment **3**. (A) Schematic free energy as a function of a joint binding and folding reaction coordinate. (B) Schematic diagram projecting the association mechanisms in two-dimensional binding and folding reaction coordinates. The natural and designed peptides bind prior to folding, although the designed fragment has a more cooperative binding—folding mechanism due to its two-state folding mechanism.

in synergy with the experimental results showing again that binding kinetics and affinity of human ACE2 to spike are similar, although higher to SARS-CoV-2 than to SARS-CoV-1, correlating with the efficient spread of SARS-CoV-2 among humans.[50]

Concluding, the applied computational protocol was successful in determining binding free-energies and main residues for the binding kinetics of the natural and designed peptides in complex with both CoV1 and CoV2. The enhanced binding energy of the designed fragment was stated to be related to the increasing contacts of the secondary loop region, which switched the folding mechanism to two-state-like, in contrast to the downhill-folder natural peptides. In addition, the inserted loop sequence conferred to **3** a tight bounding with the two spike-RBDs, explained by the increased hydrogen bonds and polar contacts. It is important to remember that the theoretical protocol is a simplified all-atom model based on the protein—peptide experimental structure with no electrostatic potential term and without solutes included, and they are implicit on the functional Hamiltonian. These assumptions make the model fast to run when compared with traditional molecular dynamics simulations, which allows many different inhibitor peptides to be evaluated against the novel coronavirus protein targets. Notwithstanding, the model is extremely versatile and these features or many others could be included to evaluate their influence on the association dynamics. The design of new potent peptides and biomolecules that inhibit novel coronaviruses can be advantageous to the development of diagnosis, vaccines, and epidemic surveillance in the years to follow.[125]

METHODS

Simulation and Analysis Details. Protein dimers were simulated with all heavy (nonhydrogen) atoms with the structure-based model (SBM),[126] also known as the Gō-model.[23] SBMs define the energy minimum of the Hamiltonian function as the native conformation; thus, SBM is a topology-based model.[76] The simulation protocol was based on the previous work[26] with GROMACS suite 5.1.4.[127] Input files for the SBM simulations were prepared with SMOG2 version 2.3-β with standard options for the all-atom model.[128] Disulfide bridges between the two cysteine residues (SS-bond) were included as a regular covalent SBM bond, which represents an

SS-bond oxidized state.[129] Native structures were analyzed by FoldX[130] to minimize residue side-chain energy.

For each system simulated, the thermodynamic analysis was performed over 40 temperature runs from lower temperatures (fully folded and on states) to higher temperatures (off states), including the transition temperature between the on and off states (T_{bind}), by the weighted histogram analysis method (WHAM)[117] with a Python script, the PyWham package.[131] The WHAM computes the microcanonical density of states that is used to build the free-energy profiles. T_b was defined as the temperature related to the specific heat peak between binding states for each protein. The number/fraction of native contacts within a given structure (Q) was used to evaluate nativeness as the reaction coordinate, which describes how similar is a given structure with respect to the initial native structure.[132] Root-mean-square fluctuation (rmsf), the radius of gyration (R_g), root-mean-square deviation (rmsd), and distance between the two chains (d) were computed with the analysis package contained in the GROMACS suite. Each simulation was executed over 1 μs with integration steps of 2 fs and snapshots of 4 ps. The all-heavy-atom SBM simulations were executed using periodic boundary conditions with no constraint on the distance between the two molecules. Enough sampling for the statistical calculations of bound/unbound states was achieved at T_{bind} and temperatures in its vicinity.

Sequence alignment and secondary structure elements were identified using the ENDscript 2 web server.[133] Interfaces and interactions formed by CoV1/CoV2 and the inhibitors were analyzed using the PISA (protein interfaces, surfaces, and assemblies) server of the European Bioinformatics Institute (EBI) (http://www.ebi.ac.uk/msd-srv/prot_int/cgi-bin/piserver).[95] Protein-energy frustration was obtained by submitting the native conformation to the AWSEM-MD Frustratometer[96,97] web server (http://frustratometer.qb.fcen.uba.ar). Protein structures were visualized with PyMOL (https://pymol.org), VMD,[134] and UCSF Chimera[135] softwares. Two- and three-dimensional curves were plotted using Grace (https://plasma-gate.weizmann.ac.il/Grace), Gnuplot (http://www.gnuplot.info), and Matplotlib[136] packages. The contact probability maps were generated using the code available at https://github.com/ronaldolab/pyContactProbability.

ASSOCIATED CONTENT

AUTHOR INFORMATION

Corresponding Author

Ronaldo Junio de Oliveira − *Laboratório de Biofísica Teórica, Departamento de Física, Instituto de Ciências Exatas, Naturais e Educação, Universidade Federal do Triângulo Mineiro, Uberaba, MG 38064-200, Brazil;* Ⓞ orcid.org/0000-0003-4860-309X; Email: ronaldo.oliveira@uftm.edu.br

Authors

Frederico Campos Freitas − *Laboratório de Biofísica Teórica, Departamento de Física, Instituto de Ciências Exatas, Naturais e Educação, Universidade Federal do Triângulo Mineiro, Uberaba, MG 38064-200, Brazil;* Ⓞ orcid.org/0000-0001-9195-9900

Paulo Henrique Borges Ferreira − *Laboratório de Biofísica Teórica, Departamento de Física, Instituto de Ciências Exatas, Naturais e Educação, Universidade Federal do Triângulo Mineiro, Uberaba, MG 38064-200, Brazil*

Denize Cristina Favaro − *Departamento de Química Orgânica, Instituto de Química, Universidade Estadual de Campinas, São Paulo, SP 13083-970, Brazil;* Ⓞ orcid.org/0000-0001-5563-2548

Complete contact information is available at:
https://pubs.acs.org/10.1021/acs.jcim.0c01320

Author Contributions

§F.C.F. and P.H.B.F. contributed equally.

Notes

The authors declare no competing financial interest.

ACKNOWLEDGMENTS

REFERENCES

(1) Kirchdoerfer, R. N.; Ward, A. B. Structure of the SARS-CoV nsp12 polymerase bound to nsp7 and nsp8 co-factors. *Nat. Commun.* **2019**, *10*, No. 2342.

(2) Gordon, C. J.; Tchesnokov, E. P.; Feng, J. Y.; Porter, D. P.; Gotte, M. The antiviral compound remdesivir potently inhibits RNA-dependent RNA polymerase from Middle East respiratory syndrome coronavirus. *J. Biol. Chem.* **2020**, *295*, 4773−4779.

(3) Yan, R.; Zhang, Y.; Li, Y.; Xia, L.; Guo, Y.; Zhou, Q. Structural basis for the recognition of SARS-CoV-2 by full-length human ACE2. *Science* **2020**, *367*, 1444−1448.

(4) Wrapp, D.; Wang, N.; Corbett, K. S.; Goldsmith, J. A.; Hsieh, C.-L.; Abiona, O.; Graham, B. S.; McLellan, J. S. Cryo-EM structure of the 2019-nCoV spike in the prefusion conformation. *Science* **2020**, *367*, 1260−1263.

(5) Zeng, Z.; Deng, F.; Shi, K.; Ye, G.; Wang, G.; Fang, L.; Xiao, S.; Fu, Z.; Peng, G. Dimerization of Coronavirus nsp9 with Diverse Modes Enhances Its Nucleic Acid Binding Affinity. *J. Virol.* **2018**, *92*, No. e00692.

(6) Chan, J. F.-W.; Kok, K.-H.; Zhu, Z.; Chu, H.; Yuan, K. K.-W.; Yuen, S.; Genomic, K.-Y. Genomic characterization of the 2019 novel human-pathogenic coronavirus isolated from a patient with atypical pneumonia after visiting Wuhan. *Emerging Microbes Infect.* **2020**, *9*, 221−236.

(7) Wu, F.; Zhao, S.; Yu, B.; Chen, Y.-M.; Wang, W.; Song, Z.-G.; Hu, Y.; Tao, Z.-W.; Tian, J.-H.; Pei, Y.-Y.; Yuan, M.-L.; Zhang, Y.-L.; Dai, F.-H.; Liu, Y.; Wang, Q.-M.; Zheng, J.-J.; Xu, L.; Holmes, E. C.; Zhang, Y.-Z. A new coronavirus associated with human respiratory disease in China. *Nature* **2020**, *579*, 265−269.

(8) Simmons, G.; Zmora, P.; Gierer, S.; Heurich, A.; Pöhlmann, S. Proteolytic activation of the SARS-coronavirus spike protein: Cutting enzymes at the cutting edge of antiviral research. *Antiviral Res.* **2013**, *100*, 605−614.

(9) Belouzard, S.; Chu, V. C.; Whittaker, G. R. Activation of the SARS coronavirus spike protein via sequential proteolytic cleavage at two distinct sites. *Proc. Natl. Acad. Sci. U.S.A.* **2009**, *106*, 5871−5876.

(10) Wang, J. Fast Identification of Possible Drug Treatment of Coronavirus Disease-19 (COVID-19) through Computational Drug Repurposing Study. *J. Chem. Inf. Model.* **2020**, *60*, 3277−3286.

(11) Wolynes, P.; Onuchic, J.; Thirumalai, D. Navigating the folding routes. *Science* **1995**, *267*, 1619−1620.

(12) Baldwin, R. The nature of protein folding pathways: The classical versus the new view. *J. Biomol. NMR* **1995**, *5*, 103−109.

(13) Dill, K. A.; Bromberg, S.; Yue, K.; Chan, H. S.; Ftebig, K. M.; Yee, D. P.; Thomas, P. D. Principles of protein folding - A perspective from simple exact models. *Prot. Sci.* **1995**, *4*, 561−602.

(14) Chahine, J.; Oliveira, R. J.; Leite, V. B. P.; Wang, J. Configuration-dependent diffusion can shift the kinetic transition state and barrier height of protein folding. *Proc. Natl. Acad. Sci. U.S.A.* **2007**, *104*, 14646−14651.

(15) Wang, J.; Lu, Q.; Lu, H. Single-Molecule Dynamics Reveals Cooperative Binding-Folding in Protein Recognition. *PLoS Comput. Biol.* **2006**, *2*, No. e78.

(16) Ferreiro, D. U.; Sánchez, I. E.; de Prat Gay, G. Transition state for protein-DNA recognition. *Proc. Natl. Acad. Sci. U.S.A.* **2008**, *105*, 10797−10802.

(17) Trizac, E.; Levy, Y.; Wolynes, P. G. Capillarity theory for the fly-casting mechanism. *Proc. Natl. Acad. Sci. U.S.A.* **2010**, *107*, 2746−2750.

(18) Baxter, E. L.; Jennings, P. A.; Onuchic, J. N. Interdomain communication revealed in the diabetes drug target mitoNEET. *Proc. Natl. Acad. Sci. U.S.A.* **2011**, *108*, 5266−5271.

(19) Whitford, P. C.; Sanbonmatsu, K. Y.; Onuchic, J. N. Biomolecular dynamics: order-disorder transitions and energy land-scapes. *Rep. Prog. Phys.* **2012**, *75*, No. 076601.

(20) Chu, W.-T.; Chu, X.; Wang, J. Binding mechanism and dynamic conformational change of C subunit of PKA with different pathways. *Proc. Natl. Acad. Sci. U.S.A.* **2017**, *114*, E7959−E7968.

(21) Sharma, R.; Sancho, D. D.; Muñoz, V. Interplay between the folding mechanism and binding modes in folding coupled to binding processes. *Phys. Chem. Chem. Phys.* **2017**, *19*, 28512−28516.

(22) Bonetti, D.; Troilo, F.; Brunori, M.; Longhi, S.; Gianni, S. How Robust Is the Mechanism of Folding-Upon-Binding for an Intrinsically Disordered Protein. *Biophys. J.* **2018**, *114*, 1889−1894.

(23) Takada, S. Gō model revisited. *Biophys. Physicobiol.* **2019**, *16*, 248−255.

(24) Neelamraju, S.; Wales, D. J.; Gosavi, S. Protein energy landscape exploration with structure-based models. *Curr. Opin. Struct. Biol.* **2020**, *64*, 145−151.

(25) Dill, K. A.; MacCallum, J. L. The Protein-Folding Problem, 50 Years On. *Science* **2012**, *338*, 1042−1046.

(26) Wang, J.; Oliveira, R. J.; Chu, X.; Whitford, P. C.; Chahine, J.; Han, W.; Wang, E.; Onuchic, J. N.; Leite, V. B. P. Topography of funneled landscapes determines the thermodynamics and kinetics of protein folding. *Proc. Natl. Acad. Sci. U.S.A.* **2012**, *109*, 15763−15768.

(27) Chu, X.; Gan, L.; Wang, E.; Wang, J. Quantifying the topography of the intrinsic energy landscape of flexible biomolecular recognition. *Proc. Natl. Acad. Sci. U.S.A.* **2013**, *110*, E2352.

(28) Sturzenegger, F.; Zosel, F.; Holmstrom, E. D.; Buholzer, K. J.; Makarov, D. E.; Nettels, D.; Schuler, B. Transition path times of coupled folding and binding reveal the formation of an encounter complex. *Nat. Commun.* **2018**, *9*, No. 4708.

(29) Fischer, E. Einfluss der Configuration auf die Wirkung der Enzyme. *Ber. Dtsch. Chem. Ges.* **1894**, *27*, 2985−2993.

(30) Csermely, P.; Palotai, R.; Nussinov, R. Induced fit, conformational selection and independent dynamic segments: an extended view of binding events. *Trends Biochem. Sci.* **2010**, *35*, 539−546.

(31) Paul, F.; Noé, F.; Weikl, T. R. Identifying Conformational-Selection and Induced-Fit Aspects in the Binding-Induced Folding of PMI from Markov State Modeling of Atomistic Simulations. *J. Phys. Chem. B* **2018**, *122*, 5649−5656.

(32) Kiefhaber, T.; Bachmann, A.; Jensen, K. S. Dynamics and mechanisms of coupled protein folding and binding reactions. *Curr. Opin. Struct. Biol.* **2012**, *22*, 21−29.

(33) Wright, P. E.; Dyson, H. J. Linking folding and binding. *Curr. Opin. Struct. Biol.* **2009**, *19*, 31−38.

(34) Sugase, K.; Dyson, H. J.; Wright, P. E. Mechanism of coupled folding and binding of an intrinsically disordered protein. *Nature* **2007**, *447*, 1021−1025.

(35) Brüschweiler, S.; Schanda, P.; Kloiber, K.; Brutscher, B.; Kontaxis, G.; Konrat, R.; Tollinger, M. Direct Observation of the Dynamic Process Underlying Allosteric Signal Transmission. *J. Am. Chem. Soc.* **2009**, *131*, 3063−3068.

(36) Pazgier, M.; Liu, M.; Zou, G.; Yuan, W.; Li, C.; Li, C.; Li, J.; Monbo, J.; Zella, D.; Tarasov, S. G.; Lu, W. Structural basis for high-affinity peptide inhibition of p53 interactions with MDM2 and MDMX. *Proc. Natl. Acad. Sci. U.S.A.* **2009**, *106*, 4665−4670.

(37) Bachmann, A.; Wildemann, D.; Praetorius, F.; Fischer, G.; Kiefhaber, T. Mapping backbone and side-chain interactions in the transition state of a coupled protein folding and binding reaction. *Proc. Natl. Acad. Sci. U.S.A.* **2011**, *108*, 3952−3957.

(38) Giri, R.; Morrone, A.; Toto, A.; Brunori, M.; Gianni, S. Structure of the transition state for the binding of c-Myb and KIX highlights an unexpected order for a disordered system. *Proc. Natl. Acad. Sci. U.S.A.* **2013**, *110*, 14942−14947.

(39) Rogers, J. M.; Oleinikovas, V.; Shammas, S. L.; Wong, C. T.; de Sancho, D.; Baker, C. M.; Clarke, J. Interplay between partner and ligand facilitates the folding and binding of an intrinsically disordered protein. *Proc. Natl. Acad. Sci. U.S.A.* **2014**, *111*, 15420−15425.

(40) Schneider, R.; Maurin, D.; Communie, G.; Kragelj, J.; Hansen, D. F.; Ruigrok, R. W. H.; Jensen, M. R.; Blackledge, M. Visualizing the Molecular Recognition Trajectory of an Intrinsically Disordered Protein Using Multinuclear Relaxation Dispersion NMR. *J. Am. Chem. Soc.* **2015**, *137*, 1220−1229.

(41) Arai, M.; Sugase, K.; Dyson, H. J.; Wright, P. E. Conformational propensities of intrinsically disordered proteins influence the mechanism of binding and folding. *Proc. Natl. Acad. Sci. U.S.A.* **2015**, *112*, 9614−9619.

(42) Schmidtgall, B.; Chaloin, O.; Bauer, V.; Sumyk, M.; Birck, C.; Torbeev, V. Dissecting mechanism of coupled folding and binding of an intrinsically disordered protein by chemical synthesis of conformationally constrained analogues. *Chem. Commun.* **2017**, *53*, 7369−7372.

(43) Lindström, I.; Dogan, J. Native Hydrophobic Binding Interactions at the Transition State for Association between the TAZ1 Domain of CBP and the Disordered TAD-STAT2 Are Not a Requirement. *Biochemistry* **2017**, *56*, 4145−4153.

(44) Han, J.; Kim, I.; Park, J.-H.; Yun, J.-H.; Joo, K.; Kim, T.; Park, G.-Y.; Ryu, K.-S.; Ko, Y.-J.; Mizutani, K.; Park, S.-Y.; Seong, R. H.; Lee, J.; Suh, J.-Y.; Lee, W. A Coil-to-Helix Transition Serves as a Binding Motif for hSNF5 and BAF155 Interaction. *Int. J. Mol. Sci.* **2020**, *21*, 2452.

(45) Antoszewski, A.; Feng, C.-J.; Vani, B. P.; Thiede, E. H.; Hong, L.; Weare, J.; Tokmakoff, A.; Dinner, A. R. Insulin Dissociates by Diverse Mechanisms of Coupled Unfolding and Unbinding. *J. Phys. Chem. B* **2020**, *124*, 5571−5587.

(46) Robustelli, P.; Piana, S.; Shaw, D. E. Mechanism of Coupled Folding-upon-Binding of an Intrinsically Disordered Protein. *J. Am. Chem. Soc.* **2020**, *142*, 11092−11101.

(47) Kim, J.-Y.; Chung, H. S. Disordered proteins follow diverse transition paths as they fold and bind to a partner. *Science* **2020**, *368*, 1253−1257.

(48) Liu, C.; Zhou, Q.; Li, Y.; Garner, L. V.; Watkins, S. P.; Carter, L. J.; Smoot, J.; Gregg, A. C.; Daniels, A. D.; Jervey, S.; Albaiu, D. Research and Development on Therapeutic Agents and Vaccines for COVID-19 and Related Human Coronavirus Diseases. *ACS Cent. Sci.* **2020**, *6*, 315−331.

(49) Whisenant, J.; Burgess, K. Blocking Coronavirus 19 Infection via the SARS-CoV-2 Spike Protein: Initial Steps. *ACS Med. Chem. Lett.* **2020**, *11*, 1076−1078.

(50) Walls, A. C.; Park, Y.-J.; Tortorici, M. A.; Wall, A.; McGuire, A. T.; Veesler, D. Structure, Function, and Antigenicity of the SARS-CoV-2 Spike Glycoprotein. *Cell* **2020**, *183*, 1735.

(51) Lan, J.; Ge, J.; Yu, J.; Shan, S.; Zhou, H.; Fan, S.; Zhang, Q.; Shi, X.; Wang, Q.; Zhang, L.; Wang, X. Structure of the SARS-CoV-2 spike receptor-binding domain bound to the ACE2 receptor. *Nature* **2020**, *581*, 215−220.

(52) Quinlan, B. D.; Mou, H.; Zhang, L.; Guo, Y.; He, W.; Ojha, A.; Parcells, M. S.; Luo, G.; Li, W.; Zhong, G.; Choe, H.; Farzan, M. *The SARS-CoV-2 receptor-binding domain elicits a potent neutralizing response without antibody-dependent enhancement*; preprint, 2020.

(53) Wang, C.; Li, W.; Drabek, D.; Okba, N. M. A.; van Haperen, R.; Osterhaus, A. D. M. E.; van Kuppeveld, F. J. M.; Haagmans, B. L.; Grosveld, F.; Bosch, B.-J. A human monoclonal antibody blocking SARS-CoV-2 infection. *Nat. Commun.* **2020**, *11*, No. 2251.

(54) Yan, R.; Zhang, Y.; Li, Y.; Xia, L.; Guo, Y.; Zhou, Q. Structural basis for the recognition of the SARS-CoV-2 by full-length human ACE2. *Science* **2020**, *367*, 1444−1448.

(55) Huang, X.; Pearce, R.; Zhang, Y. De novo design of protein peptides to block association of the SARS-CoV-2 spike protein with human ACE2. *Aging* **2020**, *12*, 11263−11276.

(56) Song, Y.; Song, J.; Wei, X.; Huang, M.; Sun, M.; Zhu, L.; Lin, B.; Shen, H.; Zhu, Z.; Yang, C. Discovery of Aptamers Targeting Receptor-Binding Domain of the SARS-CoV-2 Spike Glycoprotein. *Anal. Chem.* **2020**, *92*, 9895−9900.

(57) Letko, M.; Marzi, A.; Munster, V. Functional assessment of cell entry and receptor usage for SARS-CoV-2 and other lineage B betacoronaviruses. *Nat. Microbiol.* **2020**, *5*, 562−569.

(58) Wan, Y.; Shang, J.; Graham, R.; Baric, R. S.; Li, F. Receptor Recognition by the Novel Coronavirus from Wuhan: an Analysis Based on Decade-Long Structural Studies of SARS Coronavirus. *J. Virol.* **2020**, *94*, e00127.

(59) Wang, Q.; Zhang, Y.; Wu, L.; Niu, S.; Song, C.; Zhang, Z.; Lu, G.; Qiao, C.; Hu, Y.; Yuen, K.-Y.; Wang, Q.; Zhou, H.; Yan, J.; Qi, J.

Structural and Functional Basis of SARS-CoV-2 Entry by Using Human ACE2. *Cell* **2020**, *181*, 894−904.e9.

(60) Shang, J.; Ye, G.; Shi, K.; Wan, Y.; Luo, C.; Aihara, H.; Geng, Q.; Auerbach, A.; Li, F. Structural basis of receptor recognition by SARS-CoV-2. *Nature* **2020**, *581*, 221−224.

(61) Li, F. Structure of SARS Coronavirus Spike Receptor-Binding Domain Complexed with Receptor. *Science* **2005**, *309*, 1864−1868.

(62) Hwang, W. C.; Lin, Y.; Santelli, E.; Sui, J.; Jaroszewski, L.; Stec, B.; Farzan, M.; Marasco, W. A.; Liddington, R. C. Structural Basis of Neutralization by a Human Anti-severe Acute Respiratory Syndrome Spike Protein Antibody, 80R. *J. Biol. Chem.* **2006**, *281*, 34610−34616.

(63) Prabakaran, P.; Gan, J.; Feng, Y.; Zhu, Z.; Choudhry, V.; Xiao, X.; Ji, X.; Dimitrov, D. S. Structure of Severe Acute Respiratory Syndrome Coronavirus Receptor-binding Domain Complexed with Neutralizing Antibody. *J. Biol. Chem.* **2006**, *281*, 15829−15836.

(64) Pak, J. E.; Sharon, C.; Satkunarajah, M.; Auperin, T. C.; Cameron, C. M.; Kelvin, D. J.; Seetharaman, J.; Cochrane, A.; Plummer, F. A.; Berry, J. D.; Rini, J. M. Structural Insights into Immune Recognition of the Severe Acute Respiratory Syndrome Coronavirus S Protein Receptor Binding Domain. *J. Mol. Biol.* **2009**, *388*, 815−823.

(65) Yuan, Y.; Cao, D.; Zhang, Y.; Ma, J.; Qi, J.; Wang, Q.; Lu, G.; Wu, Y.; Yan, J.; Shi, Y.; Zhang, X.; Gao, G. F. Cryo-EM structures of MERS-CoV and SARS-CoV spike glycoproteins reveal the dynamic receptor binding domains. *Nat. Commun.* **2017**, *8*, No. 15092.

(66) Kirchdoerfer, R. N.; Wang, N.; Pallesen, J.; Wrapp, D.; Turner, H. L.; Cottrell, C. A.; Corbett, K. S.; Graham, B. S.; McLellan, J. S.; Ward, A. B. Stabilized coronavirus spikes are resistant to conformational changes induced by receptor recognition or proteolysis. *Sci. Rep.* **2018**, *8*, No. 15701.

(67) Spinello, A.; Saltalamacchia, A.; Magistrato, A. Is the Rigidity of SARS-CoV-2 Spike Receptor-Binding Motif the Hallmark for Its Enhanced Infectivity? Insights from All-Atom Simulations. *J. Phys. Chem. Lett.* **2020**, *11*, 4785−4790.

(68) Zhang, G.; Pomplun, S.; Loftis, A. R.; Tan, X.; Loas, A.; Pentelute, B. L. *Investigation of ACE2 N-terminal fragments binding to SARS-CoV-2 Spike RBD*; preprint, 2020.

(69) Qiao, B.; Olvera de la Cruz, M. Enhanced Binding of SARS-CoV-2 Spike Protein to Receptor by Distal Polybasic Cleavage Sites. *ACS Nano* **2020**, *14*, 10616−10623.

(70) Amin, M.; Sorour, M. K.; Kasry, A. Comparing the Binding Interactions in the Receptor Binding Domains of SARS-CoV-2 and SARS-CoV. *J. Phys. Chem. Lett.* **2020**, *11*, 4897−4900.

(71) Renzi, F.; Ghersi, D. *ACE2 fragment as a decoy for novel SARS-Cov-2 virus*; preprint, 2020.

(72) Han, Y.; Král, P. Computational Design of ACE2-Based Peptide Inhibitors of SARS-CoV-2. *ACS Nano* **2020**, *14*, 5143−5147.

(73) Lupala, C. S.; Li, X.; Lei, J.; Chen, H.; Qi, J.; Liu, H.; Su, X.-d. *Computational simulations reveal the binding dynamics between human ACE2 and the receptor binding domain of SARS-CoV-2 spike protein*; preprint, 2020.

(74) Wang, Y.; Liu, M.; Gao, J. Enhanced receptor binding of SARS-CoV-2 through networks of hydrogen-bonding and hydrophobic interactions. *Proc. Natl. Acad. Sci. U.S.A.* **2020**, *117*, 13967−13974.

(75) Othman, H.; Bouslama, Z.; Brandenburg, J.-T.; da Rocha, J.; Hamdi, Y.; Ghedira, K.; Srairi-Abid, N.; Hazelhurst, S. Interaction of the spike protein RBD from SARS-CoV-2 with ACE2: Similarity with SARS-CoV, hot-spot analysis and effect of the receptor polymorphism. *Biochem. Biophys. Res. Commun.* **2020**, *527*, 702−708.

(76) Clementi, C.; Nymeyer, H.; Onuchic, J. Topological and energetic factors: What determines the structural details of the transition state ensemble and "en-route" intermediates for protein folding? An investigation for small globular proteins. *J. Mol. Biol.* **2000**, *298*, 937−953.

(77) Roy, S.; Jaiswar, A.; Sarkar, R. Dynamic Asymmetry Exposes 2019-nCoV Prefusion Spike. *J. Phys. Chem. Lett.* **2020**, *11*, 7021−7027.

(78) Hoffmann, M.; Kleine-Weber, H.; Schroeder, S.; Krüger, N.; Herrler, T.; Erichsen, S.; Schiergens, T. S.; Herrler, G.; Wu, N.-H.; Nitsche, A.; Müller, M. A.; Drosten, C.; Pöhlmann, S. SARS-CoV-2 Cell Entry Depends on ACE2 and TMPRSS2 and Is Blocked by a Clinically Proven Protease Inhibitor. *Cell* **2020**, *181*, 271−280.e8.

(79) Malonis, R. J.; Lai, J. R.; Vergnolle, O. Peptide-Based Vaccines: Current Progress and Future Challenges. *Chem. Rev.* **2020**, *120*, 3210−3229.

(80) Tanaka, P.; Santos, J.; Oliveira, E.; Miglioli, N.; Assis, A.; Monteleone-Cassiano, A.; Ribeiro, V.; Duarte, M.; Machado, M.; Mascarenhas, R.; Souza, A.; Brito, L.; Oliveira, L.; Donadi, E.; Passos, G. *A Crispr-Cas9 System Designed to Introduce Point Mutations into the Human ACE2 Gene to Weaken the Interaction of the ACE2 Receptor with the SARS-CoV-2 S Protein*; preprint, 2020.

(81) Samrat, S. K.; Tharappel, A. M.; Li, Z.; Li, H. Prospect of SARS-CoV-2 spike protein: Potential role in vaccine and therapeutic development. *Virus Res.* **2020**, *288*, No. 198141.

(82) Cao, L.; Goreshnik, I.; Coventry, B.; Case, J. B.; Miller, L.; Kozodoy, L.; Chen, R. E.; Carter, L.; Walls, A. C.; Park, Y.-J.; Strauch, E.-M.; Stewart, L.; Diamond, M. S.; Veesler, D.; Baker, D. De novo design of picomolar SARS-CoV-2 miniprotein inhibitors. *Science* **2020**, *370*, 426−431.

(83) Batista, M. N.; da Silva Sanches, P. R.; Carneiro, B. M.; Braga, A. C. S.; Campos, G. R. F.; Cilli, E. M.; Rahal, P. GA-Hecate antiviral properties on HCV whole cycle represent a new antiviral class and open the door for the development of broad spectrum antivirals. *Sci. Rep.* **2018**, *8*, No. 14329.

(84) Xia, S.; Liu, M.; Wang, C.; Xu, W.; Lan, Q.; Feng, S.; Qi, F.; Bao, L.; Du, L.; Liu, S.; Qin, C.; Sun, F.; Shi, Z.; Zhu, Y.; Jiang, S.; Lu, L. Inhibition of SARS-CoV-2 (previously 2019-nCoV) infection by a highly potent pan-coronavirus fusion inhibitor targeting its spike protein that harbors a high capacity to mediate membrane fusion. *Cell Res.* **2020**, *30*, 343−355.

(85) Mycroft-West, C. J.; Su, D.; Pagani, I.; Rudd, T. R.; Elli, S.; Gandhi, N. S.; Guimond, S. E.; Miller, G. J.; Meneghetti, M. C. Z.; Nader, H. B.; Li, Y.; Nunes, Q. M.; Procter, P.; Mancini, N.; Clementi, M.; Bisio, A.; Forsyth, N. R.; Ferro, V.; Turnbull, J. E.; Guerrini, M.; Fernig, D. G.; Vicenzi, E.; Yates, E. A.; Lima, M. A.; Skidmore, M. A. Heparin Inhibits Cellular Invasion by SARS-CoV-2: Structural Dependence of the Interaction of the Spike S1 Receptor-Binding Domain with Heparin. *Thromb. Haemostasis* **2020**, *120*, 1700−1715.

(86) Elnagdy, S.; AlKhazindar, M. The Potential of Antimicrobial Peptides as an Antiviral Therapy against COVID-19. *ACS Pharmacol. Transl. Sci.* **2020**, *3*, 780−782.

(87) Vuong, W.; Khan, M. B.; Fischer, C.; Arutyunova, E.; Lamer, T.; Shields, J.; Saffran, H. A.; McKay, R. T.; van Belkum, M. J.; Joyce, M. A.; Young, H. S.; Tyrrell, D. L.; Vederas, J. C.; Lemieux, M. J. Feline coronavirus drug inhibits the main protease of SARS-CoV-2 and blocks virus replication. *Nat. Commun.* **2020**, *11*, No. 4282.

(88) Weiss, C.; Carriere, M.; Fusco, L.; Capua, I.; Regla-Nava, J. A.; Pasquali, M.; Scott, J. A.; Vitale, F.; Unal, M. A.; Mattevi, C.; Bedognetti, D.; Merkoçi, A.; Tasciotti, E.; Yilmazer, A.; Gogotsi, Y.; Stellacci, F.; Delogu, L. G. Toward Nanotechnology-Enabled Approaches against the COVID-19 Pandemic. *ACS Nano* **2020**, *14*, 6383−6406.

(89) Chauhan, G.; Madou, M. J.; Kalra, S.; Chopra, V.; Ghosh, D.; Martinez-Chapa, S. O. Nanotechnology for COVID-19: Therapeutics and Vaccine Research. *ACS Nano* **2020**, *14*, 7760−7782.

(90) Tarek, M.; Elhefnawi, M.; Maricato, J. T.; Diaz, R. S.; Shytaj, I. L.; Savarino, A. *Custommune: a web tool to design personalized and population-targeted vaccine epitopes*; preprint, 2020.

(91) Baig, M. S.; Alagumuthu, M.; Rajpoot, S.; Saqib, U. Identification of a Potential Peptide Inhibitor of SARS-CoV-2 Targeting its Entry into the Host Cells. *Drugs R&D* **2020**, *20*, 161−169.

(92) Gupta, E.; Mishra, R. K.; Niraj, R. R. K. *Identification of potential vaccine candidates against itSARS-CoV-2, A step forward to fight novel coronavirus 2019-nCoV: A Reverse Vaccinology Approach*; preprint, 2020.

(93) Pomplun, S.; Jbara, M.; Quartararo, A. J.; Zhang, G.; Brown, J. S.; Lee, Y.-C.; Ye, X.; Hanna, S.; Pentelute, B. L. De Novo Discovery of High-Affinity Peptide Binders for the SARS-CoV-2 Spike Protein. *ACS Cent. Sci.* **2021**, *7*, 156−163.

(94) Han, D. P.; Penn-Nicholson, A.; Cho, M. W. Identification of critical determinants on ACE2 for SARS-CoV entry and development of a potent entry inhibitor. *Virology* **2006**, *350*, 15−25.

(95) Krissinel, E.; Henrick, K. Inference of Macromolecular Assemblies from Crystalline State. *J. Mol. Biol.* **2007**, *372*, 774−797.

(96) Jenik, M.; Parra, R. G.; Radusky, L. G.; Turjanski, A.; Wolynes, P. G.; Ferreiro, D. U. Protein frustratometer: a tool to localize energetic frustration in protein molecules. *Nucleic Acids Res.* **2012**, *40*, W348−W351.

(97) Parra, R. G.; Schafer, N. P.; Radusky, L. G.; Tsai, M.-Y.; Guzovsky, A. B.; Wolynes, P. G.; Ferreiro, D. U. Protein Frustratometer 2: a tool to localize energetic frustration in protein molecules, now with electrostatics. *Nucleic Acids Res.* **2016**, *44*, W356−W360.

(98) Shoemaker, B. A.; Portman, J. J.; Wolynes, P. G. Speeding molecular recognition by using the folding funnel: The fly-casting mechanism. *Proc. Natl. Acad. Sci. U.S.A.* **2000**, *97*, 8868−8873.

(99) Pierse, C. A.; Dudko, O. K. Kinetics and Energetics of Biomolecular Folding and Binding. *Biophys. J.* **2013**, *105*, L19−L22.

(100) Levy, Y.; Wolynes, P. G.; Onuchic, J. N. Protein topology determines binding mechanism. *Proc. Natl. Acad. Sci. U.S.A.* **2004**, *101*, 511−516.

(101) Levy, Y.; Cho, S.; Onuchic, J.; Wolynes, P. A survey of flexible protein binding mechanisms and their transition states using native topology based energy landscapes. *J. Mol. Biol.* **2005**, *346*, 1121−1145.

(102) Linhananta, A.; Zhou, Y. The role of sidechain packing and native contact interactions in folding: Discontinuous molecular dynamics folding simulations of an all-atom Gō model of fragment B of Staphylococcal protein A. *J. Chem. Phys.* **2002**, *117*, 8983.

(103) Yao, J.; Wang, J. Neither Two-State nor Three-State: Dimerization of Lambda Cro Repressor. *J. Phys. Chem. Lett.* **2015**, *6*, 2022−2026.

(104) Chong, S.-H.; Im, H.; Ham, S. Explicit Characterization of the Free Energy Landscape of pKID-KIX Coupled Folding and Binding. *ACS Cent. Sci.* **2019**, *5*, 1342−1351.

(105) Das, A.; Yadav, A.; Gupta, M.; Purushotham, R.; Terse, V. L.; Vishvakarma, V.; Singh, S.; Nandi, T.; Mandal, K.; Gosavi, S.; Das, R.; Koti Ainavarapu, S. R.; Maiti, S. *Rational design of protein-specific folding modifiers*; preprint, 2020.

(106) Oliveberg, M.; Wolynes, P. The Experimental Survey of Protein-Folding Energy Landscape. *Quart. Rev. Biophys.* **2005**, *38*, 245−288.

(107) Toto, A.; Malagrinò, F.; Visconti, L.; Troilo, F.; Pagano, L.; Brunori, M.; Jemth, P.; Gianni, S. Templated folding of intrinsically disordered proteins. *J. Biol. Chem.* **2020**, *295*, 6586−6593.

(108) Crabtree, M. D.; Mendonça, C. A. T. F.; Bubb, Q. R.; Clarke, J. Folding and binding pathways of BH3-only proteins are encoded within their intrinsically disordered sequence, not templated by partner proteins. *J. Biol. Chem.* **2018**, *293*, 9718−9723.

(109) Javaheri, M. R. H.; Chamberlin, R. V. A free-energy landscape picture and Landau theory for the dynamics of disordered materials. *J. Chem. Phys.* **2006**, *125*, No. 154503.

(110) Lu, G.; Wang, Q.; Gao, G. F. Bat-to-human: spike features determining 'host jump' of coronaviruses SARS-CoV, MERS-CoV, and beyond. *Trends Microbiol.* **2015**, *23*, 468−478.

(111) Ortega, J. T.; Serrano, M. L.; Pujol, F. H.; Rangel, H. R. Role of changes in SARS-CoV-2 spike protein in the interaction with the human ACE2 receptor: An in silico analysis. *EXCLI J.* **2020**, *19*, 410−417.

(112) Giron, C. C.; Laaksonen, A.; Barroso da Silva, F. L. On the interactions of the receptor-binding domain of SARS-CoV-1 and SARS-CoV-2 spike proteins with monoclonal antibodies and the receptor ACE2. *Virus Res.* **2020**, *285*, No. 198021.

(113) Barnes, C. O.; West, A. P.; Huey-Tubman, K. E.; Hoffmann, M. A.; Sharaf, N. G.; Hoffman, P. R.; Koranda, N.; Gristick, H. B.; Gaebler, C.; Muecksch, F.; Lorenzi, J. C. C.; Finkin, S.; Hägglöf, T.; Hurley, A.; Millard, K. G.; Weisblum, Y.; Schmidt, F.; Hatziioannou, T.; Bieniasz, P. D.; Caskey, M.; Robbiani, D. F.; Nussenzweig, M. C.; Bjorkman, P. J. Structures of Human Antibodies Bound to SARS-CoV-2 Spike Reveal Common Epitopes and Recurrent Features of Antibodies. *Cell* **2020**, *182*, 828−842.e16.

(114) Shammas, S. L.; Travis, A. J.; Clarke, J. Remarkably Fast Coupled Folding and Binding of the Intrinsically Disordered Transactivation Domain of cMyb to CBP KIX. *J. Phys. Chem. B* **2013**, *117*, 13346−13356.

(115) Rogers, J. M.; Steward, A.; Clarke, J. Folding and Binding of an Intrinsically Disordered Protein: Fast, but Not 'Diffusion-Limited. *J. Am. Chem. Soc.* **2013**, *135*, 1415−1422.

(116) Du, X.; Li, Y.; Xia, Y.-L.; Ai, S.-M.; Liang, J.; Sang, P.; Ji, X.-L.; Liu, S.-Q. Insights into Protein−Ligand Interactions: Mechanisms, Models, and Methods. *Int. J. Mol. Sci.* **2016**, *17*, 144.

(117) Ferrenberg, A. M.; Swendsen, R. H. New Monte Carlo technique for studying phase transitions. *Phys. Rev. Lett.* **1988**, *61*, 2635−2638.

(118) Krämer, S. D.; Wöhrle, J.; Rath, C.; Roth, G. Anabel: An Online Tool for the Real-Time Kinetic Analysis of Binding Events. *Bioinf. Biol. Insights* **2019**, *13*, No. 117793221882138.

(119) Pomplun, S. Targeting the SARS-CoV-2-spike protein: from antibodies to miniproteins and peptides. *RSC Med. Chem.* **2021**, DOI: 10.1039/D0MD00385A.

(120) Walls, A. C.; Xiong, X.; Park, Y.-J.; Tortorici, M. A.; Snijder, J.; Quispe, J.; Cameroni, E.; Gopal, R.; Dai, M.; Lanzavecchia, A.; Zambon, M.; Rey, F. A.; Corti, D.; Veesler, D. Unexpected Receptor Functional Mimicry Elucidates Activation of Coronavirus Fusion. *Cell* **2019**, *176*, 1026−1039.e15.

(121) Chan, K. K.; Dorosky, D.; Sharma, P.; Abbasi, S. A.; Dye, J. M.; Kranz, D. M.; Herbert, A. S.; Procko, E. Engineering human ACE2 to optimize binding to the spike protein of SARS coronavirus 2. *Science* **2020**, *369*, 1261−1265.

(122) Glasgow, A.; Glasgow, J.; Limonta, D.; Solomon, P.; Lui, I.; Zhang, Y.; Nix, M. A.; Rettko, N. J.; Zha, S.; Yamin, R.; Kao, K.; Rosenberg, O. S.; Ravetch, J. V.; Wiita, A. P.; Leung, K. K.; Lim, S. A.; Zhou, X. X.; Hobman, T. C.; Kortemme, T.; Wells, J. A. Engineered ACE2 receptor traps potently neutralize SARS-CoV-2. *Proc. Natl. Acad. Sci. U.S.A.* **2020**, *117*, 28046−28055.

(123) Linsky, T. W.; Vergara, R.; Codina, N.; Nelson, J. W.; Walker, M. J.; Su, W.; Barnes, C. O.; Hsiang, T.-Y.; Esser-Nobis, K.; Yu, K.; Reneer, Z. B.; Hou, Y. J.; Priya, T.; Mitsumoto, M.; Pong, A.; Lau, U. Y.; Mason, M. L.; Chen, J.; Chen, A.; Berrocal, T.; Peng, H.; Clairmont, N. S.; Castellanos, J.; Lin, Y.-R.; Josephson- Day, A.; Baric, R. S.; Fuller, D. H.; Walkey, C. D.; Ross, T. M.; Swanson, R.; Bjorkman, P. J.; Gale, M.; Blancas-Mejia, L. M.; Yen, H.-L.; Silva, D.-A. De novo design of potent and resilient hACE2 decoys to neutralize SARS-CoV-2. *Science* **2020**, *370*, 1208−1214.

(124) Shah, M.; Moon, S. U.; Woo, H. G. *Pharmacophore-based peptide biologics neutralize SARS-CoV-2 S1 and deter S1-ACE2 interaction in vitro*; preprint, 2020.

(125) Nash, B.; Badea, A.; Reddy, A.; Bosch, M.; Salcedo, N.; Gomez, A. R.; Versiani, A.; Dutra Silva, G. C.; Lopes dos Santos, T. M. I.; Milhim, B. H. G. A.; Moraes, M. M.; Fernandes Campos, G. R.; Quieroz, F.; Negri Reis, A. F.; Nogueira, M. L.; Naumova, E. N.; Bosch, I.; Herrera, B. B. *The impact of high frequency rapid viral antigen screening on COVID-19 spread and outcomes: a validation and modeling study*; preprint, 2020.

(126) Whitford, P.; Noel, J.; Gosavi, S.; Schug, A.; Sanbonmatsu, K.; Onuchic, J. An all-atom structure-based potential for proteins: Bridging minimal models with all-atom empirical forcefields. *Proteins: Struct., Funct., Bioinf.* **2009**, *75*, 430−441.

(127) van der Spoel, D.; Lindahl, E.; Hess, B.; Groenhof, G.; Mark, A.; Berendsen, H. GROMACS: Fast, flexible, and free. *J. Comput. Chem.* **2005**, *26*, 1701−1718.

(128) Noel, J. K.; Levi, M.; Raghunathan, M.; Lammert, H.; Hayes, R. L.; Onuchic, J. N.; Whitford, P. C. SMOG 2: A Versatile Software Package for Generating Structure-Based Models. *PLoS Comput. Biol.* **2016**, *12*, No. e1004794.

(129) Haglund, E.; Sułkowska, J. I.; He, Z.; Feng, G.-S.; Jennings, P. A.; Onuchic, J. N. The Unique Cysteine Knot Regulates the Pleotropic Hormone Leptin. *PLoS One* **2012**, *7*, No. e45654.

(130) Schymkowitz, J.; Borg, J.; Stricher, F.; Nys, R.; Rousseau, F.; Serrano, L. The FoldX web server: an online force field. *Nucleic Acids Res.* **2005**, *33*, W382−W388.

(131) Sun, L.; Noel, J. K.; Sulkowska, J. I.; Levine, H.; Onuchic, J. N. Connecting Thermal and Mechanical Protein (Un)folding Landscapes. *Biophys. J.* **2014**, *107*, 2950−2961.

(132) Cho, S. S.; Levy, Y.; Wolynes, P. G. P versus Q: Structural reaction coordinates capture protein folding on smooth landscapes. *Proc. Natl. Acad. Sci. U.S.A.* **2006**, *103*, 586−591.

(133) Robert, X.; Gouet, P. Deciphering key features in protein structures with the new ENDscript server. *Nucleic Acids Res.* **2014**, *42*, W320−W324.

(134) Humphrey, W.; Dalke, A.; Schulten, K. VMD: Visual Molecular Dynamics. *J. Mol. Graphics* **1996**, *14*, 33−38.

(135) Pettersen, E. F.; Goddard, T. D.; Huang, C. C.; Couch, G. S.; Greenblatt, D. M.; Meng, E. C.; Ferrin, T. E. UCSF Chimera-a visualization system for exploratory research and analysis. *J. Comput. Chem.* **2004**, *25*, 1605−1612.

(136) Hunter, J. D. Matplotlib: A 2D graphics environment. *Comput. Sci. Eng.* **2007**, *9*, 90−95.